Urban Climate 44 (2022) 101215

Contents lists available at ScienceDirect

Urban Climate

journal homepage: www.elsevier.com/locate/uclim

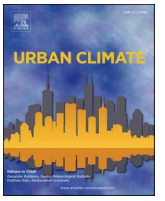

A mechanistic assessment of urban heat island intensities and drivers across climates

Ziyan Zhang [a,*,1], Athanasios Paschalis [a], Ana Mijic [a], Naika Meili [b], Gabriele Manoli [c], Maarten van Reeuwijk [a], Simone Fatichi [b]

[a] Department of Civil and Environmental Engineering, Imperial College London, UK
[b] Department of Civil and Environmental Engineering, National University of Singapore, Singapore
[c] Department of Civil, Environmental and Geomatic Engineering, University College London, UK

ARTICLE INFO

Keywords:
Urban heat island
Land surface modelling
Remote sensing
Urban greening
Urban heat island mitigation strategies

ABSTRACT

The urban heat island effect (UHI) has been widely observed globally, causing climate, health, and energy impacts in cities. The UHI intensities have been found to largely depend on background climate and the properties of the urban fabric. Yet, a complete mechanistic understanding of how UHIs develop at a global scale is still missing. Using an urban ecohydrological and land-surface model (urban Tethys-Chloris) in combination with multi-source remote sensing data, we performed simulations for 49 large urban clusters across the Northern Hemisphere in 2009–2019 and analysed how surface and canopy air UHIs (SUHI and CUHI, respectively) develop during day and night. Biophysical drivers triggering the development of SUHIs and CUHIs have similar dependencies on background climate, but with different magnitudes. In humid regions daytime UHIs can be largely explained by the urban-rural difference in evapotranspiration, whereas heat convection and conduction are important in arid areas. Plant irrigation can largely promote daytime urban evapotranspiration only in arid and semi-arid climates. During night, heat conduction from the urban fabric to the environment creates large UHIs mostly in warm arid regions. Overall, this study presents a mechanistic quantification of how UHIs develop worldwide and proposes viable solutions for sustainable climate-sensitive mitigation strategies.

Abbreviations: ϕ_s, soil water potential; AC, air conditioning; CUHI, canopy layer air urban heat island; $CUHI_d$, average daytime canopy urban heat island intensity; $CUHI_n$, average night-time canopy urban heat island intensity; ET, evapotranspiration including evaporation and transpiration; LAI, leaf area index; LUCY, the Large Scale Urban Consumption of Energy Model; R^2, the coefficient of determination; REF, simulation performed for the rural state; RMSE, the root mean squared error; SuDS, Sustainable Urban Drainage Systems; SUHI, surface urban heat island; $SUHI_h$, surface urban heat island derived from the horizontal urban surface temperature viewed from above (ground, roofs and tree); $SUHI_p$, surface urban heat island derived from the ground-level pedestrian urban surface temperature (ground, building walls and tree); UHI, urban heat island; UHI_d, average daytime urban heat island; UHI_n, average nighttime urban heat island; URB, simulation performed for the urban state; URB_{bu}, a part of Simulation URB, which specifically represents the built-up area; URB_{pk}, a part of Simulation URB, which specifically represents the urban park (or, forested) area; UT&C, Urban Tethys-Chloris – an urban ecohydrological model; V_{cmax}, the maximum photosynthetic carboxylation rate of vegetation; WI, wetness index; ΔET, the urban-rural difference in evapotranspiration; ΔLAI, the urban-rural difference in vegetation leaf area index; ΔT_c, urban-rural difference in canyon air temperature (i.e., canopy layer air urban heat island intensity); ΔT_s, urban-rural difference in surface temperature (i.e., surface urban heat island intensity).

* Corresponding author.
E-mail address: ziyan.zhang14@imperial.ac.uk (Z. Zhang).
[1] Present address: Room 302, Skempton Building, Department of Civil and Environmental Engineering, Imperial College London, London SW7 2AZ.

https://doi.org/10.1016/j.uclim.2022.101215
Received 2 December 2021; Received in revised form 19 May 2022; Accepted 10 June 2022
Available online 18 June 2022

1. Introduction

The urban heat island (UHI) effect, produced by increasing urbanization, has become a major concern for the deterioration of life quality of urban dwellers over the last two decades (Arnfield, 2003). The UHI effect can be defined as the canopy layer air temperature or surface temperature difference between the urban environment and its surrounding rural area (Oke, 1982, 1995; Oke et al., 2017). UHIs develop due to differences in the energy balance between the city and its surroundings (e.g., Oke et al., 2017; Manoli et al., 2020), further triggering changes in atmospheric circulation (Omidvar et al., 2020; Fan et al., 2017; Zhang et al., 2014). Such differences are caused by the urban fabric and anthropogenic activities that simultaneously alter the surface and air radiative properties, the balance between sensible and latent heat fluxes, and add excess heat to the surface and air budget (Oke, 1982, 1995).

The intensity of surface UHIs (SUHIs) on a global scale has been found to depend on the city's background climate, with summertime SUHIs increasing with annual precipitation and in some cases temperature (Zhao et al., 2014; Li et al., 2019; Zhou et al., 2016b). To explain the mechanisms behind SUHI intensities, many previous studies used satellite observations of surface temperatures (Peng et al., 2012; Zhou et al., 2013; Liao et al., 2018; Paschalis et al., 2021; Zhou et al., 2018). Urban-rural contrasts in evapotranspiration (ET) and/or heat convection efficiency have been found to be the main determinants of daytime SUHI intensities during summer, and their relative importance depends on the background climatic conditions (Li et al., 2019; Zhao et al., 2014; Manoli et al., 2019; Paschalis et al., 2021). However, satellite sensors can mostly quantify nadir viewing temperatures and thus cannot fully represent the complete urban surface temperature within its complex three dimensional geometry (Yang et al., 2020a, 2020b; Yang et al., 2021). Hence, quantification of the land surface fluxes leading to the SUHI development in urban environments is not straightforward. There is currently very limited availability of energy flux measurements that are collected within cities or at the top of buildings. Some exceptions exist for major cities, e.g., Melbourne, Phoenix AZ, Helsinki, Basel, and Shanghai to name a few, where eddy-covariance measurement towers have been installed within the urban area (Zhang and Zhang, 2015; Wood et al., 2013; Kotthaus and Grimmond, 2012; Templeton et al., 2018; Chow et al., 2014; Schmutz et al., 2016), but overall the attribution of the mechanisms leading to the observed SUHI patterns has been a major challenge.

Compared to SUHIs, canopy air UHI (CUHI) is more relevant to human outdoor thermal comfort (Ho et al., 2016). It is thus important to understand in detail also the dynamics leading to the CUHI development. Many in-situ observations have shown that SUHIs and CUHIs are two different quantities. Generally, SUHI and CUHI are known to have opposite diurnal patterns (Wang et al., 2017; Chakraborty et al., 2017). The SUHI and CUHI developments share some similar biophysical drivers but have different magnitudes (Venter et al., 2021). Observation-based quantification of CUHIs requires in-situ data of canopy air temperatures within and around a city, commonly available from official weather stations (Cui and De Foy, 2012; Sun et al., 2020) or crowdsourced citizen weather stations, albeit commonly with lower quality (Venter et al., 2021; Chapman et al., 2017; Varentsov et al., 2020). Such data is however very limited for global scale studies.

To overcome such data limitations, urban models of different complexities have been developed and can be used to understand the SUHIs and CUHIs (Zhao et al., 2014; Li et al., 2019; Gu and Li, 2018; Broadbent et al., 2018) by explicitly resolving the land surface energy budget and the atmospheric dynamics of the boundary layer within a city. A major limitation of some models has been the lack of detailed representation of urban vegetation within the cities. The interactions between vegetation and the built environment have been identified as a crucial factor to properly quantify the urban land surface energy balance (Grimmond et al., 2010). As urban vegetation can affect temperature via shading, modifying roughness and evaporative cooling which can be further amplified by irrigation (Ziter et al., 2019; Rahman et al., 2019; Zhang et al., 2021; Grylls and van Reeuwijk, 2021; Chow et al., 2011; Meili et al., 2021b), it is crucial that vegetation processes within cities are properly represented in models.

New generation urban canopy models have now start including detailed representations of urban vegetation (Huang et al., 2021; Wang et al., 2021; Moradi et al., 2022; Krayenhoff et al., 2020; Meili et al., 2020). The explicitly modelled vegetation dynamics include, for example, the tree shading on urban built surfaces, plant responses to the urban microclimate and vegetation management such as irrigation. Arguably one of the most detailed descriptions of vegetation processes in an urban canyon model has been included in Urban Tethys-Chloris (UT&C) (Meili et al., 2021a; Meili et al., 2020; Meili et al., 2021b), a novel model that has been successfully applied at multiple sites in different climates (i.e., Singapore, Melbourne, Phoenix) to investigate the role of vegetation in urban microclimate. Models like UT&C require detailed information regarding the properties of the urban fabric including city geometry and plant traits. Model application with a global focus can now be performed due to new streams of remote sensing data that can contribute information to parametrize urban land surface models, from detailed geometries of all buildings within a city (Li et al., 2020) to leaf area dynamics (Fuster et al., 2020), plant traits (Walker et al., 2017; Bassiouni et al., 2020), and vegetation dynamics (Paschalis et al., 2021).

In this study, we use the state-of-art urban ecohydrological model UT&C to investigate the drivers of SUHI and CUHI development in 49 northern hemisphere large city clusters during the period 2009–2019. A new model parametrization protocol was developed that leverages information from multiple remote sensing data products. Using this framework, we investigate the dominant biophysical mechanisms controlling summer UHI. Specifically, we partition the role of urban vegetation, its irrigation management, the influence of anthropogenic activities, and the properties of the urban fabric that lead to the SUHI and CUHI development, during both day and night, and provide a mechanistic explanation for the dependence of each component on background climate.

2. Data and methods

2.1. Study sites

We selected 49 large urban clusters located in Europe ($N = 20$), the USA ($N = 26$) and China ($N = 3$) and different climates (Fig. 1, Table S1). The reasons for selecting these cities are: 1) the availability of data for model parameterization and validation; and, 2) the relatively small fraction (0.2 ± 0.2) of intense agriculture (mostly rainfed) around the urban clusters with overall small impacts on daytime land surface temperature (Table S1, Fig. S1), as rural agriculture and its irrigation has been found to be important in some areas (Kumar et al., 2017; Zhou et al., 2016b). The climates of the selected cities are in Group B (Arid), Group C (Temperate) and Group D (Continental) based on the Köppen–Geiger classification (Kottek et al., 2006). In Fig. 1, cities in temperate climates (Group C) are further sub-divided into two different types based on whether summer is relatively dry or not. The selected temperate cities are mainly located in wet summer climates, while some cities in the western US ($N = 4$) and southern Europe (N = 2) are located in dry/semi-dry regions.

2.2. Numerical experiments

2.2.1. Model description

We used the mechanistic urban ecohydrological model Urban Tethys-Chloris (Meili et al., 2020), to resolve the water and surface energy balance for all 49 city clusters (Fig. 1, Table S1). In UT&C, the urban geometry is that of an urban canyon, specified with two buildings of identical height and given orientation, canyon width, and roof width. The trees, if present, are assumed in two uniform strips along the street canyon. The ground surface can be divided into three fractions of impervious, bare and/or vegetated surfaces; the roof area can be divided into two surface types, impervious and/or vegetated. The model accounts for urban vegetation including trees, low stature ground vegetation, and green roofs by using a mechanistic modelling framework that includes plant physiological responses to environmental forcing, such as plant stomata regulation by light, temperature, vapor pressure deficit and soil moisture (Paschalis et al., 2018; Moustakis et al., 2022; Fatichi et al., 2012a, 2012b). UT&C simulates radiation redistribution within the urban canyon using a Monte Carlo ray tracing algorithm. Specifically, the reflection of shortwave and longwave radiation within the urban canyon is calculated from reciprocal view factors between the surfaces, and the surfaces and the sky, which are computed with a Monte-Carlo ray tracing approach (Howell, 1969, 1998; Wang, 2014; Frank et al., 2016). Tree transmissivity for direct shortwave radiation is calculated as a function of leaf area index (LAI) and an optical transmissivity coefficient using the Beer-Lambert law (De Pury and Farquhar, 1997). Prognostic surface temperatures within the computational domain include, impervious/vegetated roof surfaces, impervious/bare/vegetated ground surfaces, sunlit/sun-shaded wall surfaces and tree canopy, and they are computed by solving the energy balance, i.e., net radiation, latent and sensible heat fluxes, and conductive heat fluxes in the ground and wall layers.

Turbulence within the canyon is resolved as a function of the canyon geometry and accounting for the effect of trees on the wind profile, which depends on canopy characteristics (i.e., tree height, radius, LAI). Aerodynamic resistance for stable, unstable, or neutral

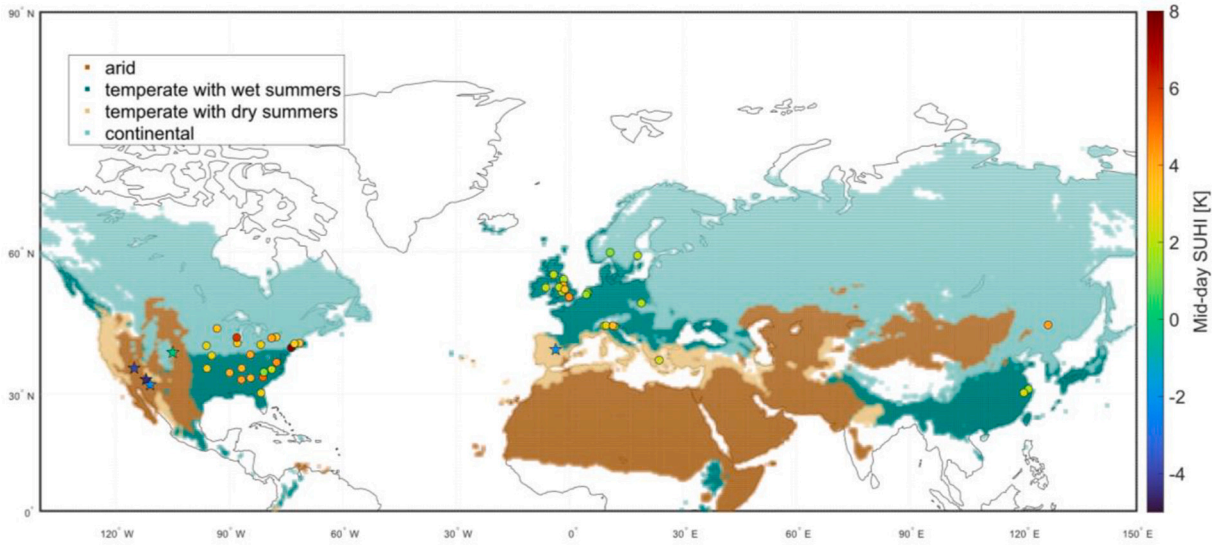

Fig. 1. The map of the 49 case studies. Map colours correspond to the Köppen climate zones with: dark brown, arid climates (BWh, BWk, BSh, BSk); light brown, temperate climates with dry summers (Csa, Csb, Csc); light green, continental climates (Dwa, Dwb, Dwc, Dwd, Dfa, Dfb, Dfc, Dfd); dark green, temperate climates with wet summers (Cwa, Cwb, Cwc, Cfa, Cfb, Cfc). Circle and star shapes represent, respectively, cities with positive and negative mid-day SUHI intensity during summer. The scatter colour indicates the magnitude of summer mid-day SUHI intensity from satellite observations. (For interpretation of the references to colour in this figure legend, the reader is referred to the web version of this article.)

atmosphere above the canyon is estimated with a simplified Monin–Obukhov similarity theory according to Mascart et al. (1995). Additional resistances to heat fluxes are considered both vertically i.e., from the ground to canyon air (Mahat et al., 2013) and horizontally, i.e., from wall to canyon air (Rowley et al., 1930; Rowley and Eckley, 1932). Stomatal resistances for roof and ground vegetated surfaces and tree cover depend on plant photosynthetic activity and follow the Leuning scheme (Leuning, 1995; Paschalis et al., 2017; Fatichi et al., 2012a), assuming a two big-leaf (sunlit and shaded) approach for vegetated fractions. Urban transpiration from trees and ground vegetation is simulated with a biochemical model of photosynthesis, which takes into account the photosynthetic active radiation, vapor pressure deficit, and available soil moisture that plant roots can access.

The inputs required to force the model are hourly downwelling shortwave and longwave radiation, precipitation, air temperature, humidity, wind speed, and atmospheric pressure at the reference height above canyon, as well as the sum of anthropogenic heat emitted by all urban activities such as air conditioning, car exhaust and human metabolism. The conductive heat exchanged by regulating indoor temperatures (i.e., domestic cooling or heating) is implicitly simulated in the model. In our study, the interior building temperature was set to be a maximum of 26 °C if air conditioning (AC) is in use during summer and/or a minimum of 18 °C if heating is in use during winter; building interior temperature equals the air temperature at atmospheric reference height in other cases.

2.2.2. Simulation set-up

Lumped simulations were performed for all cities (Simulation URB), where a city was described as a built-up area consisting of an urban canyon (Simulation URB_{bu}), representative of the city's geometry (i.e., buildings, roads and pavements) with street trees and local small gardens, and a large green area without buildings (Simulation URB_{pk}), representative of the green open spaces (e.g., parks). For every city, a reference simulation (Simulation REF) was also performed corresponding to the city's surrounding rural area (Supplementary Section S2.0).

Specifically, Simulation URB_{bu} used a representative canyon geometry for each city; whereas Simulation URB_{pk} was assumed as a wide (100 m of width) and shallow (5 m of height) 'canyon' covered by grasses and trees only. To account for multiple canyon orientations within a city, three different orientations (0, 45 and 90°(s) from North) were simulated for the urban canyons, and the results were averaged across these simulations by weighting the simulation of 45° with a weight of 2 to also take into account the direction of 135° which was found to have minor effect. The other two setups were only considered in the North-South orientation, due to their wide and shallow geometry and orientation effects are negligible. Overall, the simulated temperature and fluxes of a whole city cluster (X_{URB}) can be expressed as:

$$X_{URB} = (1-\mu)\frac{\sum_{i=0,45,45,90} X_{URB_{bu}^{i}}}{4} + \mu X_{URB_{pk}} \quad (1)$$

where, μ is the urban park fraction within the urban cluster; i represents the canyon orientations within the city, X_{URB} represents any temperature or flux we will report for the entire canyon and X_{URBbu}, X_{URBpk} represent the corresponding variables for the built-up and urban park simulation respectively.

A climate dependent irrigation and anthropogenic heat were applied within cities for both the built-up area (Simulation URB_{bu}) and the urban park (Simulation URB_{pk}). Specifically, urban vegetation is actively managed within all cities under dry climates (WI < 0.6, where WI is the wetness index defined as the ratio of annual precipitation over annual potential evapotranspiration), but not in the reference simulation (REF). Additionally, irrigation was applied only during the vegetation growing seasons (from May to October) at a 3 mm/h rate and only if the soil water potential is less than −0.1 MPa for trees and − 0.3 MPa for grasses. The irrigation rate was chosen to be representative of common sprinkler irrigation systems (Volo et al., 2014) and water potential thresholds are high enough to avoid any vegetation water stress. Neither irrigation nor anthropogenic heat emissions were considered in the surrounding regions (Simulation REF), otherwise these shared the same setups as the Simulation URB_{pk}. General information on the simulation setups is summarized in Table 1.

2.2.3. Data

Meteorological forcing for a 11-year period of 2009–2019 for all variables needed to run the model were obtained from the ERA5-Land reanalysis product (Muñoz Sabater, 2019). The atmospheric CO_2 concentration was set as a constant at 400 ppm to avoid any feedback related to increasing CO_2.

Table 1
Summary of the three simulations setups used for each city in the analysis.

	Urban Simulations (URB)		Reference Simulation (REF)
	Built-up (URB_{bu})	Urban Parks (URB_{pk})	
Domain	City cluster		0.1 degrees of buffer zone (~10 km) around the city cluster
Irrigation	3 mm/h if required; only applied in dry regions (WI < 0.6)		No
Anthropogenic Heat	Yes		No
Canyon dimensions	Representative urban geometry	100 m of canyon width 5 m of building height	100 m of canyon width 5 m of building height
Canyon orientation	0, 45, 90° from North	North-South	North-South
Ground fraction	Representative urban built-up ground cover	100% vegetated	100% vegetated
Roof fraction	100% impervious	–	–

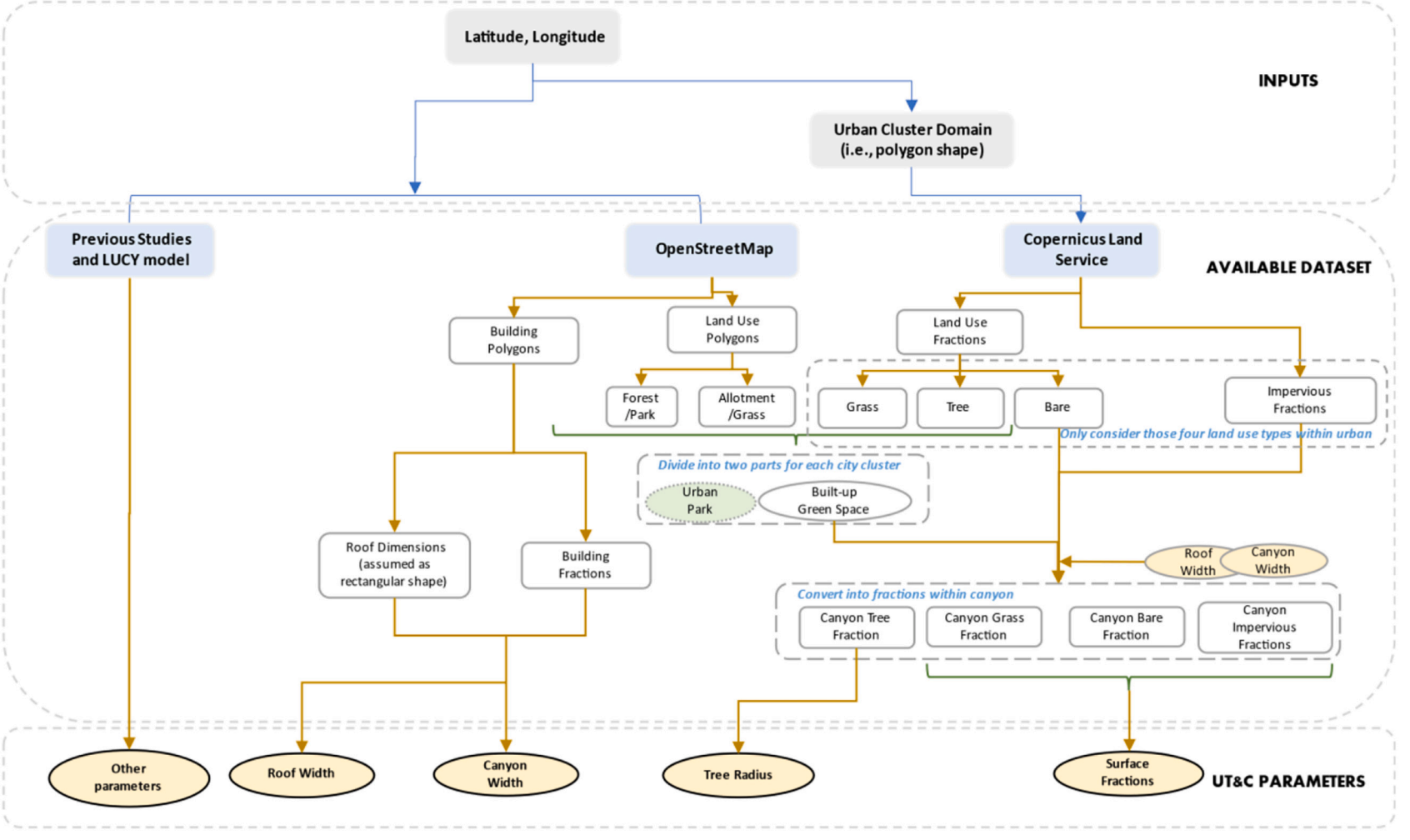

Fig. 2. Flow chart for preparing representative key parameters for each city.

City clusters were obtained from the study of Wang et al. (2019), and the rural area was defined as the buffer zone of 0.1° (i.e., approximately 10 km) surrounding the urban boundary (Supplementary Section S2.0). The average building height for each city was obtained by Li et al. (2020) for Europe, USA and China, and was used to describe the height of buildings in UT&C model. The remaining features of the canyon geometry (roof/building width, distance between adjacent buildings) were estimated based on the OpenStreetMap dataset (www.openstreetmap.org) that contains different types of land use as polygons within city clusters such as commercial and residential buildings, parks, forests, allotments, and grasslands. The flow chart shown in Fig. 2 illustrates the methodology used for estimating the representative canyon dimensions for each city. More detailed descriptions are provided in the Supplementary (Section S3.0).

To further enhance land use information, we used the 100 m resolution land cover map from the Copernicus Land Service (Buchhorn et al., 2019), derived from PROBA-V satellite observations for 2015 to estimate the percentages of bare ground, trees, and grasses over the whole city region. In this study, we assumed those covers as the only pervious fractions within cities (Fig. 2), and excluded all other types of land cover such as permanent water and crops. To derive the fraction of impervious covers, we used the high (30 m) spatial resolution dataset from Brown de Colstoun et al. (2017). Based on those surface fractions and the area ratio of parks to gardens obtained from OpenStreetMap, we further divided urban grass and tree fractions within the whole urban region into those associated with local gardens for the Simulation URB_{bu} and the others associated with large green spaces for the Simulation URB_{pk} (Fig. 2, Supplementary SectionS3.0).

Soil at the ground was assumed to be 2000 mm deep for all cities given the lack of city specific data (Shuster et al., 2021). Tree root depth and grass root depth were set to be 1000 mm and 250 mm respectively with a root density declining exponentially. Representative root depths were obtained for the most common urban tree and grass species from the TRY database (Kattge et al., 2011). We also assumed a vertically homogeneous soil profile, and used SoilGrids v2.0 dataset (de Sousa et al., 2020; Hengl et al., 2017) to estimate soil textural properties typical of each region (fractions of clay, sand, soil organic carbon content) and the Saxton and Rawls pedotransfer functions (Saxton and Rawls, 2006) to convert soil texture into soil hydraulic parameters. Free drainage at the bottom of the soil was simulated in the UT&C model and no groundwater was considered. No leakage from water pipes was considered.

Seasonally varying leaf area index (LAI) from the PROBA-V at a 300 m (version 1.0) (Fuster et al., 2020) was used for all city clusters to estimate tree and grass LAI throughout the season (Supplementary Section S4.0). The maximum photosynthetic carboxylation rate (V_{cmax}) was parametrized in our study based on the work of Walker et al. (2017), assuming it is constant across the whole city domain. This assumes that within the city vegetation has similar traits as natural vegetation in the rural surroundings of the city. The last vegetation parameter adjusted in this study is the soil water potential, ϕ_s, when plant water uptake downregulates from its maximum rate due to water stress. This was estimated based on the analysis of Bassiouni et al. (2020), again assuming that urban vegetation has similar traits to the rural surroundings.

Seasonal anthropogenic heat flux for individual cities was computed from the large scale urban consumption of energy (LUCY) model at 2.5 × 2.5 arc-minute resolution (Allen et al., 2011; Lindberg et al., 2013; Grimmond et al., 2018). We simulated the hourly urban anthropogenic heat flux for the year 2017, the year with the most high-quality data to run the LUCY model (i.e., population density, energy consumptions, transport numbers), and assumed an identical seasonal pattern in the remaining years. The building emissions, as a part of anthropogenic heat in the LUCY model, are calculated based on temperature-dependent energy demand, excluding the heat exchanges between indoor and outdoor environments. This heat flux is indeed implicitly simulated as the conductive heat flux into and out of wall and ground layers in the UT&C model.

Apart from the lumped simulations representing the average conditions of each city, we also examined spatial heterogeneity within a city and specifically for London's 32 boroughs and City of London (Greater London Authority, 2015) using the same methodology described in Fig. 2. This is to (a) estimate within-city variability and (b) to confirm that an average lumped city-scale simulation provides reasonable results when compared with the average UHI intensity from distributed simulations across the city. All other UT&C model parameters used in this study were assumed to be constants in all cities and summarized in the Supplementary Material (Section S5.0).

2.3. Simulation analyses

2.3.1. Model validation

To validate the simulated results, we calculated the 2-D horizontal surface UHI intensities ($SUHI_h$) viewed from above, using the simulated surface temperatures for the impervious roof fraction, all ground fractions and tree weighted by their plan view area (i.e., T_{plan} in Stewart et al. (2021)) (Supplementary Section S6.0). Vertical wall temperatures were not considered in the validation as the SUHI as seen by satellites is strongly affected by rooftop temperature. Model simulations were validated both for the mid-day (i.e., 12:00 noon local time) $SUHI_h$ intensity and its diurnal variability as observed by satellite remote sensing. The diurnal pattern of land surface temperature was obtained from the geostationary satellite data available by the Copernicus Global Land Service at a 5 km resolution (Freitas et al., 2013), which was further corrected based on the higher resolution 1 km MODIS AQUA(TERRA) observations (Wan et al., 2015a; Wan et al., 2015a) at 01:30 am/pm (10:30 am/pm) local time for their ascending(descending) orbits (Supplementary Section S7.0). Specifically, MODIS observations were extrapolated beyond their local observation time using the diurnal pattern from the geostationary data. The diurnal pattern of simulated $SUHI_h$ was validated in terms of Root Mean Square Error (RMSE) and the coefficient of determination (R^2) between the observed and simulated average hourly patterns of SUHI. Midday $SUHI_h$ was validated in terms of RMSE and R^2 for all MODIS observations extrapolated to 12:00 noon local time. Only the cloud free days of the simulation were used for the model validation.

To validate our London borough simulations, we used the average $SUHI_h$ estimates from Chakraborty and Lee (2019) derived using

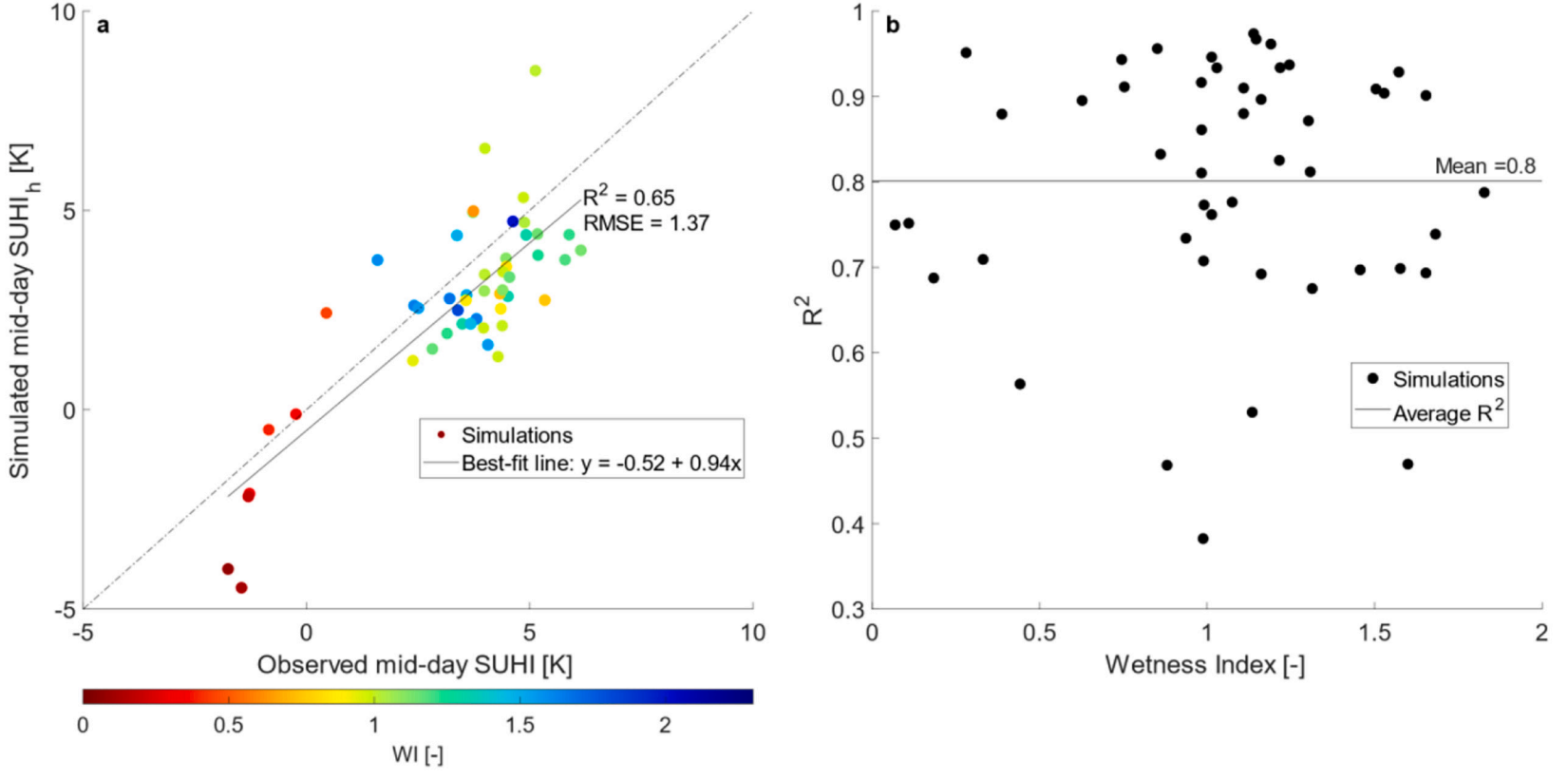

Fig. 3. (a) Comparison between observed mid-day SUHI and simulated mid-day $SUHI_h$ magnitude for all cities. Each point represents one city. Circle colours indicate the city wetness index. The dashed line indicates the 1:1 line (i.e., y = x). The solid line indicates the linear regression between observed and simulated $SUHI_h$ intensity. (b) the coefficient of determination between the observed and modelled diurnal pattern of $SUHI_h$ for all cities as a function of WI. The R^2 value is used as a measure for the fit between the simulated and observed diurnal pattern in each city and as can be seen in b) it is independent of wetness index. The solid line indicates the average R^2 value among all 49 cities. Each point represents one city.

MODIS and available via Google Earth Engine (https://yceo.users.earthengine.app/view/uhimap).

2.3.2. Urban heat island attribution

Canopy urban heat island intensity, which is more relevant to public outdoor thermal comfort than SUHI, is decomposed according to its energy budget (Supplementary Section S8.0). The magnitude of CUHI (i.e., ΔT_c) can be expressed in synthesis as Eq. (2).

$$\Delta T_c = r_{ah}\left[\frac{1}{\rho C_p}\left(\underbrace{\Delta S_n + \Delta L_n}_{\text{Net Radiation}} - \underbrace{\Delta LE}_{\text{Evapotranspiration}} - \underbrace{\Delta G}_{\text{Conduction}} + \underbrace{\Delta Q_{ah}}_{\text{Anthropogenic Heat}}\right) - \underbrace{(T_c - T_a)\Delta\frac{1}{r_{ah}}}_{\text{Above Canyon Convection}}\right] \quad (2)$$

where, T_c is canyon air temperature; T_a is atmospheric air temperature; Δ is a perturbation from the rural base state; ρ is the air density; $C_p$is the specific heat of air; S_n is the net shortwave radiation within the canyon; L_n is the net longwave radiation within the canyon; LE is the latent heat flux within the canyon; r_{ah} is the canyon aerodynamic resistance between canyon air and atmospheric air layer; G is the combination of ground and wall conductive heat flux, which thus include the heat storage effect underneath the surfaces; and Q_{ah} is the anthropogenic heat flux. The values of S_n, L_n, LE, r_{ah}, T_c and G are simulated by the UT&C model.

A similar partitioning analysis is performed for the ground-level pedestrian SUHI intensities ($SUHI_p$) using the simulated surface temperatures for all wall, ground and tree fractions (i.e., T_{ped} in Stewart et al. (2021)). A more detailed description for calculating the complete surface temperature and fluxes and partitioning $SUHI_p$ can be found in the Supplementary Material (Section S6.0 and S8.0).

2.3.3. Effects of urban irrigation

Additional simulations, where urban irrigation was either supplied in intermediate and humid climates or removed from dry climates, were also performed to quantify the effect of vegetation irrigation under different climatic conditions. We define the irrigation-induced temperature changes as the difference between average daytime CUHI intensity during summer in the urban irrigated and non-irrigated cases.

3. Results

3.1. Model validation

Fig. 3a shows the agreement ($R^2 = 0.65$, slope = 0.94) between the simulated mid-day $SUHI_h$ intensity and the observations during summer (i.e., June, July, August). Our simulations slightly underestimate $SUHI_h$ (regression slope of 0.94), which might be attributed to the choice of the same surface albedo value for roofs and streets for all case studies. Generally, cities in dry regions have smaller $SUHI_h$ and even experience urban cooling (i.e., oasis effect) at midday (Stewart et al., 2021), while cities under intermediate and

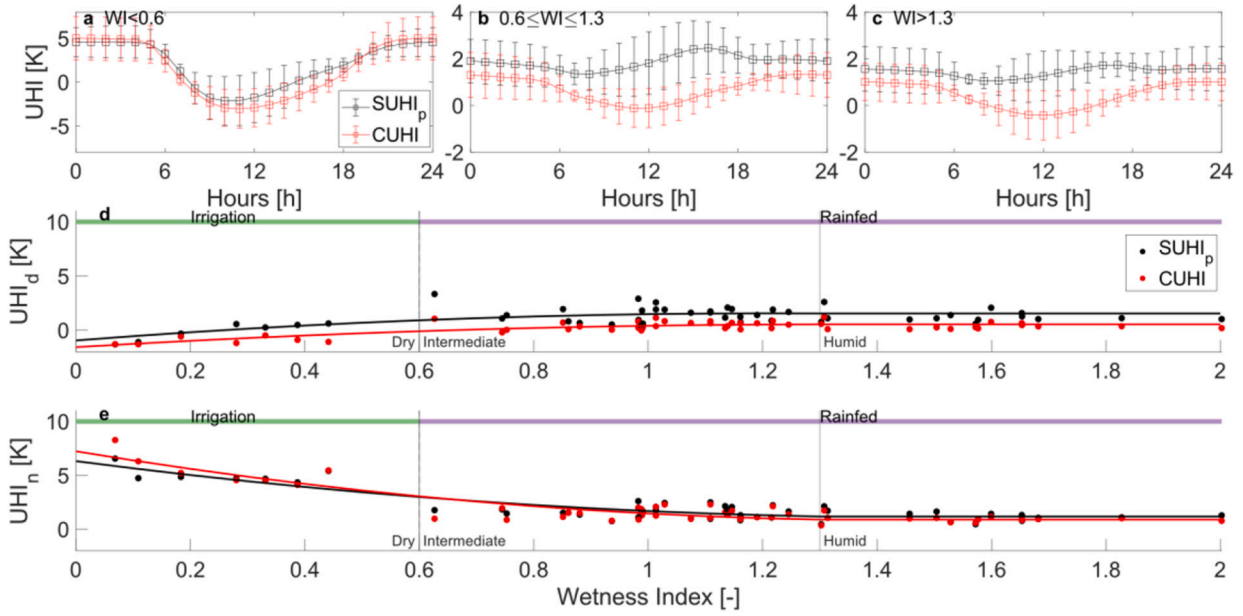

Fig. 4. (a-c) The diurnal pattern of simulated $SUHI_p$ and CUHI in different aridity levels. Errorbar represents ± 1 standard deviation. Scatter plot between the average complete $SUHI_p$ and CUHI and WI during (d) daytime and (e) nighttime in arid (Wetness Index, WI ≤ 0.6), intermediate (0.6 < WI < 1.3) and humid (WI > 1.3) climates. Each dot represents one city. The dots are fitted by the polynomial lines of order 1 or 2 (solid lines).

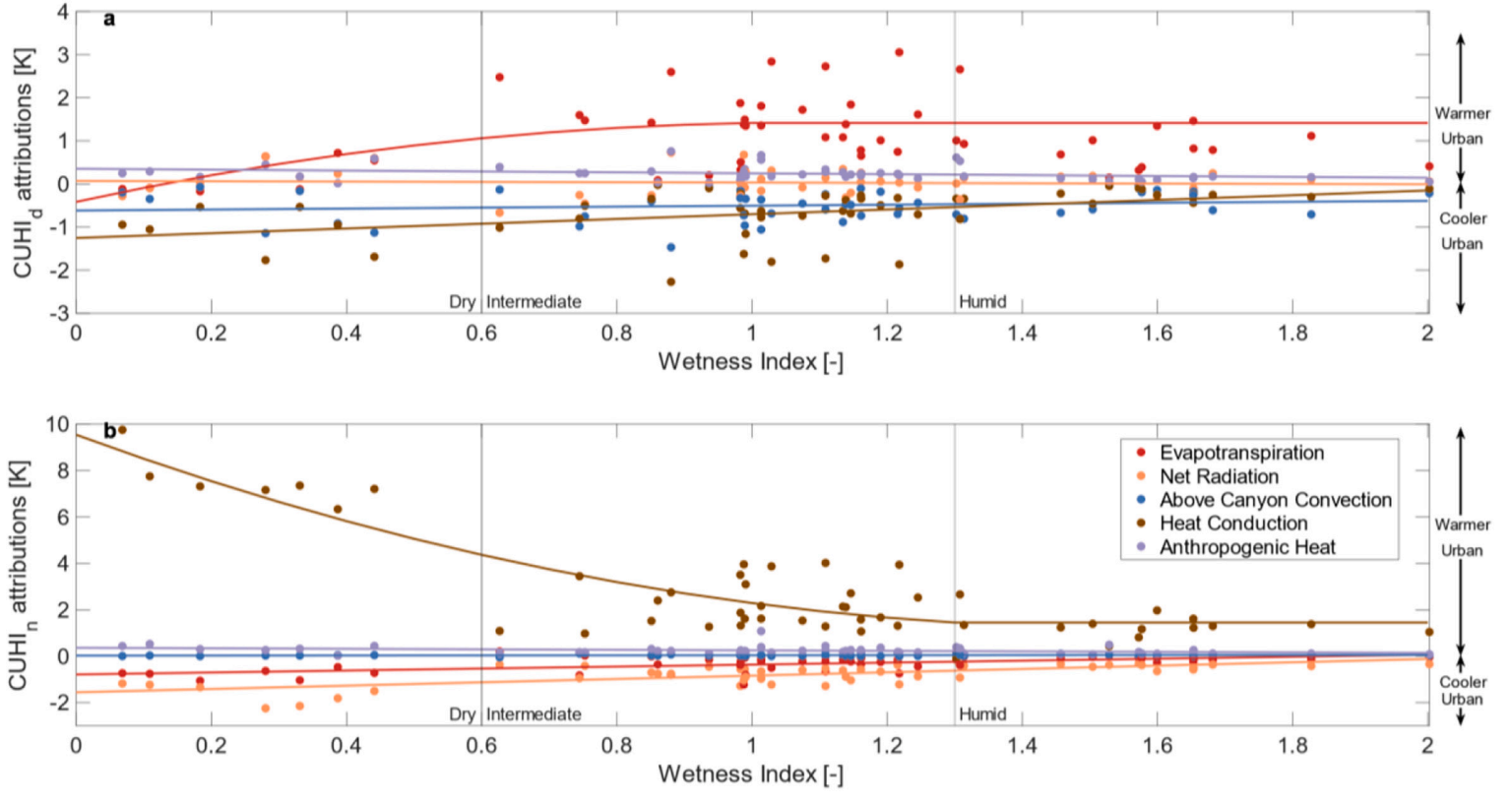

Fig. 5. The computed attributions of summer average (a) daytime and (b) nighttime CUHI intensity varying with background climates. The attribution factors are urban-rural difference in evapotranspiration, net radiation, above canyon convection efficiency, conductive heat flux and anthropogenic heat flux as shown in Eq. 2. Polynomial lines of order 1 or 2 (solid lines) are fitted to the single city results (dots).

humid climates show greater $SUHI_h$ intensities (Paschalis et al., 2021). There is also a good agreement between model and data (mean $R^2 = 0.80$, Fig. S4) regarding the diurnal pattern of $SUHI_h$ during summer, which is independent of background climate (Fig. 3b). In intermediate and wet cities, we recovered the commonly expected and observed behaviour of high daytime and low night-time $SUHI_h$ (Fig. S4). The dry cities showed the opposite pattern, which was also consistent with the satellite observations (mean $R^2 = 0.75$, Fig. 3b, Fig. S4).

3.2. UHI attribution as a function of background climate

Climatic patterns of observed and simulated summer mid-day $SUHI_h$ intensity across all 49 cities in the US, Europe, and China confirm the dependence on background climates (Fig. 1, Fig. S4) as already shown in previous studies (Manoli et al., 2019; Zhao et al., 2014; Liu et al., 2020; Gu and Li, 2018). In our simulations, $SUHI_p$ intensity is also dependent on background climate. Though, the absolute values of summer $SUHI_p$ and $SUHI_h$ are different for all climates, with large negative differences during daytime and small positive differences during nighttime (Fig. S5), which is consistent with previous findings (Stewart et al., 2021). Wetter cities in the USA generate significant mid-day $SUHI_p$ with the highest of 3.8 °C in Tulsa; while in dry climates, cities can induce urban oasis effects by up to −5.0 °C in Phoenix. A similar pattern was also found in European cities, where all dry cities (except Athens, Greece, which has the least urban greening) have negative mid-day $SUHI_p$ intensities with the lowest of −2.3 °C in Madrid (Fig. 4a). The opposite pattern occurs during night, when dry cities experience much higher mid-night (at 01:00 am Local Time) $SUHI_p$ than wetter cities which generate milder mid-night $SUHI_p$ magnitudes with an overall average of 1.3 °C. Among all dry cities, the highest mid-night $SUHI_p$ was found in Las Vegas (7.1 °C) in the US.

Different from the diurnal pattern of SUHIs (both $SUHI_h$ and $SUHI_p$), the simulated summer CUHIs have a larger magnitude during night than during daytime for more humid climates (Fig. 4b-c, Fig. S4). In dry climates, a significant mid-day urban oasis effect was found also for canopy air temperatures (−2.6 ± 4.2 °C) whereas in wet climates daytime CUHIs were insignificant (−0.03 ± 0.9 °C). During mid-night in arid climates, a very strong CUHI intensity was simulated (4.1 ± 3.4 °C) which is also positive but with lower magnitude in wetter climates (1.2 ± 0.9 °C). Even though the diurnal patterns of CUHI and $SUHI_p$ are clearly different in wetter climates, their average values follow a similar pattern with WI (Fig. 4d-e). The simulated $SUHI_p$ and CUHI intensity both show a positive and negative correlation with annual mean precipitation and air temperature during daytime, respectively, and negative and positive correlation during nighttime, respectively (Fig. S6). As it takes into account both precipitation and temperature, WI is a better predictor for average SUHIs and CUHIs than single climate variables, and both UHIs depend on WI non-linearly.

To further understand the mechanisms leading to such a pattern in summer UHI, and CUHI in particular, we quantify the importance of five drivers (evaporative cooling, net radiation, above canyon heat convection, anthropogenic heat, and conductive heat) for CUHI and four drivers (evaporative cooling, net radiation, within canyon heat convection, and conductive heat) for $SUHI_p$ based on the simulated results from the UT&C model. As both equations (Eq. 2 and Supplementary Section S8.0) used for the attribution are an approximation of the energy balance solution, we evaluated their accuracy for all cities. The approximation was good with an overall error of accuracy relative to the UT&C simulations of around 0.05 ± 0.2 K (Fig. S7). At the summertime scale (i.e., average value for June July and August), the simulated interannual $SUHI_p$ and CUHI for both daytime and nighttime are highly correlated ($R^2 = 0.89$ and $R^2 = 0.99$ respectively, Fig. S8). The average slope of the interannual linear regression during summer night (slope = 0.96) is higher than during daytime (slope = 0.74). This is because the various drivers of CUHIs and SUHIs for both day and nighttime (i.e., urban-rural difference in evapotranspiration, net radiation, heat conduction) have a similar relative importance, though with different magnitudes (Fig. 5, Fig. S9). For this reason, we will describe here only results for CUHI as similar considerations can be made for $SUHI_p$.

For daytime CUHIs, urban-rural difference in evaporative cooling was the largest factor in humid cities, whereas in dry cities heat conduction to building interiors and the ground as well as heat convection to the free atmosphere explained most of the CUHI intensities. Specifically, humid cities have much lower ET than their surroundings, which is largely a consequence of the much lower leaf area (35.0 ± 8.7% less) (Fig. S10) and greater impervious fraction within urban lands. This urban-rural temperature difference due to ET alone can explain around 1.4 ± 0.8 K of the total daytime CUHI intensity for intermediate climates and 0.9 ± 0.6 K for humid climates during summer. In more humid cities, the warming effect of urban-rural difference in evapotranspiration is partially counterbalanced by heat convection and conduction factors. In contrast, in hot and dry cities experiencing small and even negative CUHIs, the impact of urban-rural differences in evapotranspiration (ΔET) was much smaller (0.2 ± 0.4 K) because of urban irrigation. In those arid regions, heat stored in the urban fabric and lost as conductive fluxes to cooler building interiors (−1.1 ± 0.5 K) and a more efficient heat convection to the free atmosphere (−0.5 ± 0.3 K) led to an oasis effect, with the evaporative factor playing a smaller role. Compared to all other attributions mentioned above, anthropogenic heat has overall a relatively small contribution to CUHI intensity and decreases with WI, with the highest warming effect of 0.3 ± 0.2 K in dry cities during summer daytime.

The leading factor for the development of nighttime CUHIs is heat conduction due to a high release of stored heat within the urban materials to the surfaces and further toward the canyon air, inducing a significant warming effect of 7.5 ± 1.0 K in arid climates and of 1.9 ± 1.0 K in more humid climates. Differences in longwave radiation due to differences in surface temperatures contribute to a cooling effect, although of lower magnitude, mainly in arid climates (−1.6 ± 0.4 K). A small cooling effect due to ΔET was found during nighttime in dry climates (−0.8 ± 0.2 K), which is due to the irrigation applied during nighttime enhancing ground evaporation and to a smaller degree plant transpiration under high vapor pressure deficit.

3.3. Impact of irrigation on UHI development

To fully understand the impact of urban irrigation, we compared the CUHI intensities with and without irrigation for all cities and their corresponding CUHI attributions. Fig. 6 shows that the urban irrigation-induced changes in CUHI during summer vary strongly with background climate. Irrigation altered the surface energy by enhancing plant transpiration due to reduced plant water stress and by altering the thermal properties of soils (Fig. S11). Overall, the irrigation cooling effect was strongest in arid sites (-0.9 ± 0.8 K). In more humid climates, applying irrigation or not has almost no effect on the CUHI intensity (intermediate: -0.1 $\pm$ 0.1 K, humid: -0.04 $\pm$ 0.08 K) (Fig. 6b-c). Even though irrigation application can also impact surface albedo and surface emissivity due to increased soil moisture, the UT&C model does not consider those changes and we refrain from any further interpretation regarding this factor.

3.4. Within city UHI variability

Our simulations are based on a lumped modelling approach to evaluate the development of UHIs during summer. However, it is important to also quantify the expected variability of UHI intensity within the city. We further applied the same methodology at the borough scale in London. Our simulated daytime $SUHI_h$ spatial variability was consistent with satellite observations (Fig. S12). The within city variability of CUHI in London is about 29.0% and 13.0% of the total variance simulated across all cities at mid-day and mid-night during summer, respectively. The variability within London is generally higher for $SUHI_h$ than it is for CUHI and occurs mostly during the day (Fig. 7). Despite the within city variability, the diurnal and seasonal patterns were the same for all London Boroughs. Compared to the 'average' London results, $SUHI_h$ and CUHI intensities can vary by up to 1.32 K at the borough scale particularly at mid-day. This variability would likely be larger if simulations were carried out at an even finer (e.g., street level) scale but demonstrate that our lumped approach provides reasonable city average values. In fact, the city average UHI intensities, were similar in magnitude with the UHI intensity computed with an "average city" lumped parametrization. In comparison to other cities in our study, London is expected to have a high within city UHI variability as it spans a large range of both urban geometries (Fig. S13), from high rise building (i.e., City of London) to low density housing in the suburbs, and within-canyon ground vegetated fraction (i.e., excluding parks and street trees) spanning from 0.0057 (i.e., City of London) to 0.85 (i.e., Harrow).

4. Discussion

In this study we leveraged the capabilities of a state-of-the-art urban ecohydrological model, parametrized with a wide range of remotely sensed data and driven by meteorological forcing from reanalysis. The model was capable of reproducing the global spatial and temporal (i.e., diurnal) values of observed surface urban heat islands, providing mechanistic explanation for their development across climates.

Overall, the summer CUHI intensity and its key controlling factors heavily depend on background climate, particularly regional aridity, during both daytime and nighttime. We found overall larger daytime CUHIs in humid climates due to the warming effect of

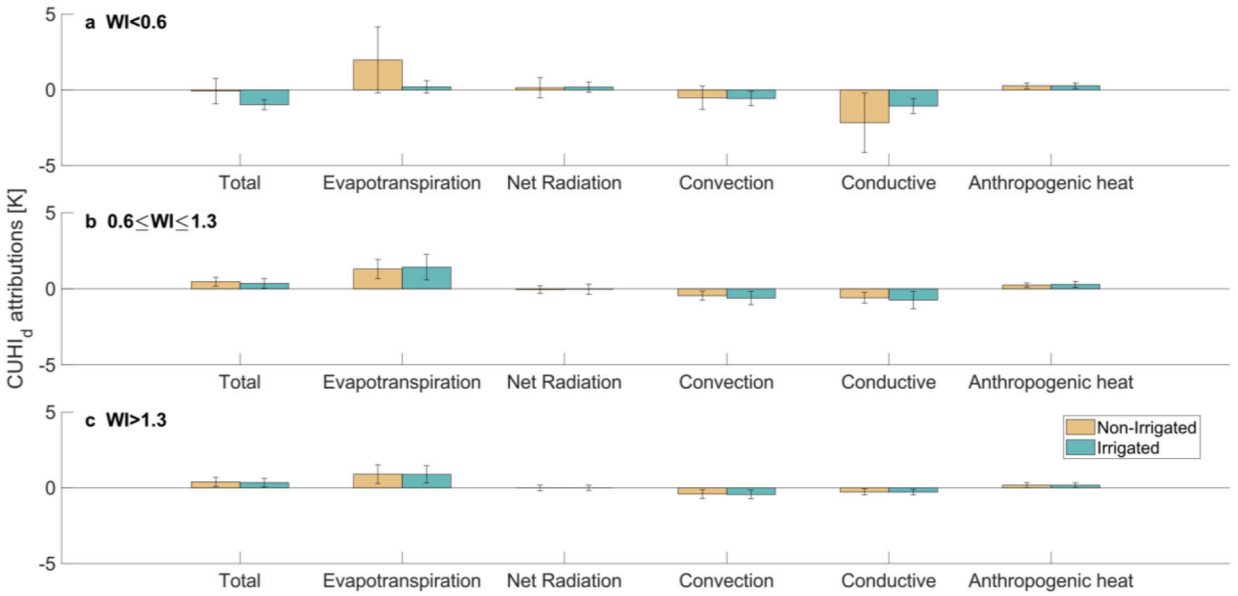

Fig. 6. (a-c) Comparisons of average daytime CUHI (Total) and its attribution factors (Evapotranspiration, Net Radiation, Above Canyon Convection Efficiency, Conductive Heat Flux and Anthropogenic Heat Flux) between irrigated and non-irrigated urban land surfaces during summer in three different climate aridity level. The errorbars represent $\pm$ 1 standard deviation.

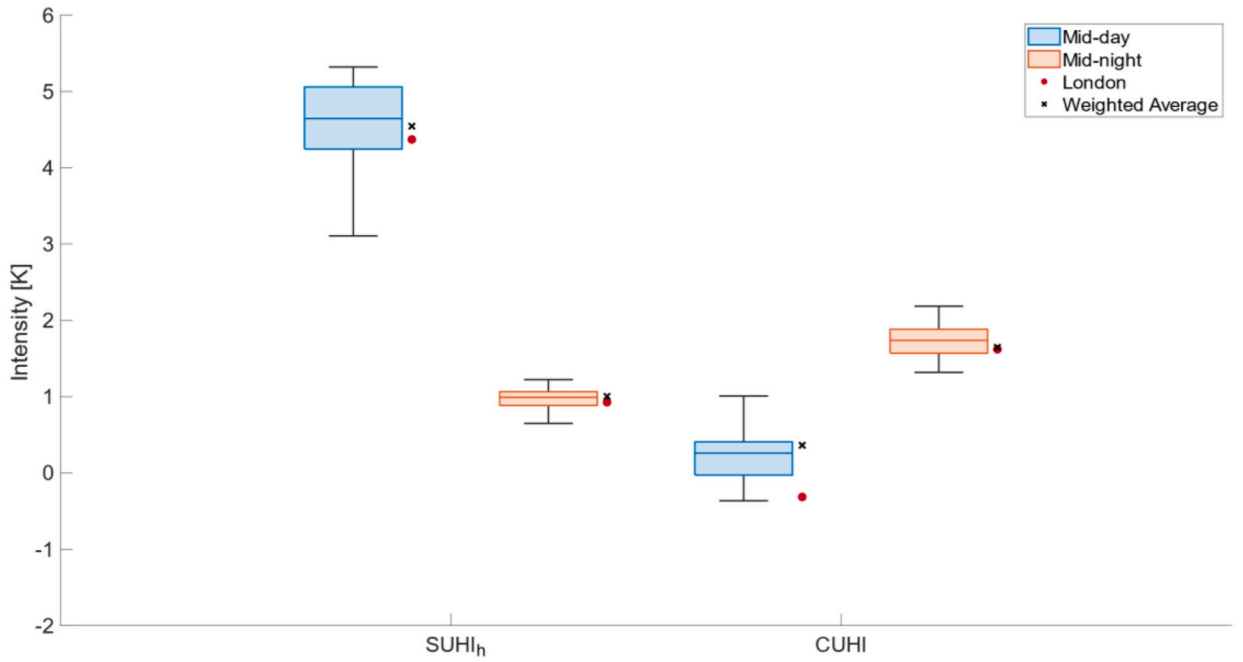

Fig. 7. The simulated summertime mid-day and mid-night $SUHI_h$ and CUHI intensities for 33 London Boroughs represented with boxplots. The circles represent the results for the 'average' London as analysed in previous sections. The crosses represent the weighted average values for Boroughs according to their areas.

ΔET which was gradually reduced in arid climates. This finding is in agreement with previous studies showing that spatial variations of summer daytime SUHI intensity were largely controlled by variations in the capacity of urban and rural areas to evaporate water, especially from dense forested areas (Manoli et al., 2019; Li et al., 2019; Zhou et al., 2014; Paschalis et al., 2021). The impact of urban greening on reducing daytime air and surface temperature may differ to some extent (Novick and Katul, 2020). These differences in our study depend on the aerodynamic resistances within and above canyon, which govern the ability to dissipate heat, and were not very pronounced, as CUHI and $SUHI_p$ have similar drivers (Fig. 5, Fig. S9). Especially in arid climates, the warming effect induced on urban canopy air during daytime by the lack of evapotranspiration was mostly counteracted by more efficient heat dissipation to the atmosphere and heat conduction to the ground and buildings in these urban areas.

The conduction heat flux into building and ground was identified as an important factor during both daytime and nighttime, which is often not fully represented in previous SUHI or CUHI studies. Either the flux was completely neglected from the biophysical drivers of SUHIs (Manoli et al., 2019), or only the ground heat flux was considered (Wang et al., 2020) which may underestimate its importance as considerable heat is transferred from and to the buildings. This clearly shows that urban canyon land surface schemes cannot neglect temperature controls of building interiors and consequently demonstrates the potential of building heating and AC in modulating outside temperature. Our study shows that conductive fluxes including all canyon surfaces provided a significant cooling effect during daytime in arid climates, in agreement with previous studies (Zhao et al., 2018; Li et al., 2019) that explicitly included heat fluxes for temperature-regulated building interiors. This result is however contradicting some studies that found either a small or negligible cooling (Fitria et al., 2019; Cao et al., 2016) or a warming effect (Zhao et al., 2014). The disagreement mainly arises from the building parameters and city morphology which have been found to significantly affect heat storage change during daytime (Chew et al., 2021; Chen et al., 2012) and may also be related to the representation of the relevant processes in the model used. Consistent with previous findings (Jacobs et al., 2018; Zhao et al., 2018; Fitria et al., 2019; Imran et al., 2019; Zhao et al., 2014; Li et al., 2019; Cao et al., 2016), our results demonstrate that during nighttime the release of urban heat stored within building and ground can induce a significant warming effect leading to large SUHI and CUHI development, especially in arid climates.

Overall, the results suggest that there is not a unique driver that is triggering SUHI and CUHI developments, and that the importance of each driver is strongly related to both the background climate and the time of day, thus the design of mitigation strategies for both UHIs should take these complex patterns into consideration.

4.1. Importance of urban management and planning

During daytime, the dominant factor determining both SUHI and CUHI (UHI_{both} hereinafter to lump the results that refer to both SUHI and CUHI values) development is the lack of urban evaporative cooling. Most of the differences in evaporative cooling can be explained by the differences in green cover and leaf area between the urban and rural areas. Those differences are largest in cities located in more humid climates as cities replaced vegetated land with high evapotranspiration potential, contrary to arid cities that

replaced sparsely vegetated or barren land. For the wet cities, increasing green cover can partially reduce UHI_{both}. In dry areas, urban green cover is comparable and, in some cases, slightly larger than the surrounding rural areas (Paschalis et al., 2021). For those arid sites, increasing urban greening can also be an efficient urban heat mitigation practice, as there is a large potential of extending the currently relatively small urban green cover. However, that would only be feasible with a concurrent provision of water for plant irrigation. In fact, as our simulations show here, evaporative cooling in arid cities is strongly enhanced only in the presence of irrigation during daytime (Yang et al., 2020a). However, the benefits of irrigation may not always counterbalance their costs especially in water scare regions (Reyes et al., 2018). Irrigation application amount and schedule as well as Sustainable Urban Drainage Systems (SuDS) are worth considering for optimal and sustainable designs especially given the uneven distribution of water (Volo et al., 2014; Howells et al., 2013; Broadbent et al., 2018; Freni and Liuzzo, 2019; Coutts et al., 2013; Hoang and Fenner, 2016; Liu and Jensen, 2018)(Hoang and Fenner, 2016; Liu and Jensen, 2018). As part of SuDS operations, collected stormwater or reclaimed wastewater can be used for irrigation of public open green spaces and urban parklands to meet most of the demands (Liu et al., 2019). Proper species selection with high drought tolerance could also partially mitigate the water scarcity problem, but they will likely reduce the cooling potential. Efficient heat convection within and above canyon can offer an overall urban cooling potential for surface and canopy air respectively. Due to the direct link with the surface roughness of the urban boundary layer, urban planning can consider optimization of the geometry of urban canyons that best dissipate heat (Yu et al., 2020). Additionally, energy consumption was found to be a factor for daytime CUHI development. In our study anthropogenic heat fluxes were warming the cities particularly in arid climates. Energy consumption explained to a large degree the anthropogenic fluxes within the LUCY model, which was used in our study (Allen et al., 2011) showing that energy management can also offer an urban heat mitigation potential.

Contrary to daytime developments, nighttime UHI_{both} are predominantly affected by heat conduction of construction materials (Imran et al., 2019). Thus, improving the design of buildings for example reduced sky view factors that minimize net radiation absorption, or advanced materials and construction solutions that avoid excess heat storage and heat release from the buildings to the canyon can offer a great urban heat mitigation potential (He, 2019; Gago et al., 2013), particularly in arid cities, where the nighttime UHI_{both} is more significant. Best selection of building materials could reduce the urban canyon air temperatures (Hamdi and Schayes, 2008) especially during nighttime when vegetation evaporative cooling is minimal also in more humid climates. In arid climates, urban vegetation with the aid of irrigation can not only provide daytime mitigation but also induce air cooling at night under high vapor pressure deficit (Ibsen et al., 2021). Though, as discussed before, water scarcity considerations would be very important.

4.2. Study limitations and perspectives

The lack of validation of CUHI intensity is one of the difficulties of studying CUHI at the global scale. A thorough global scale validation would only be possible with in situ air temperature data at high frequencies at multiple locations for all cities and their surroundings. Currently very few cities in the world are monitored at this level of detail, with a few exceptions including CUHI oriented city wide monitoring networks (Kolokotroni and Giridharan, 2008; Giannaros et al., 2018; Warren et al., 2016), which however have been mostly limited in terms of duration. Alternative sources of data to support such a validation include measurements from portable weather stations/sensors (Lin et al., 2017; Liu et al., 2017), citizen science data initiatives, e.g. the Weather Underground (Krüger and Emmanuel, 2013) and Netatmo (Varentsov et al., 2020; Meier et al., 2017; Venter et al., 2021), and even smartphone battery temperatures (Overeem et al., 2013). However, the quality of observations might prevent very accurate analyses.

Lack of data regarding key details of urban geometry and vegetation species within every city at the global scale is also a limitation of this study. Even though we used state of the art remote sensing data for both building heights and plant traits, both were retrieved at low resolutions that do not allow to resolve within city heterogeneity. Improvements in machine learning algorithms applied at very high-resolution satellite imagery can provide a way forward for estimating urban geometries in detail, including the shapes and heights of every building (Muftah et al., 2021). Those detailed 3D building geometry data can further help to sample the land surface temperature observed by the non-nadir viewing satellites. Additionally, new data from multiband aerial imagery can be used to retrieve reflectivity properties of the building roof at the global scale (Ban-Weiss et al., 2015). Another limitation of this study is the estimation of plant physiological traits. In this study urban and rural vegetation properties were considered as identical, but in reality, within the urban environment non-native species are commonly planted. Detailed knowledge of the species distribution within cities could improve the estimation of evapotranspirative cooling. However, with the exception of few cities, for example London (Greater London Authority, 2021), such information currently does not exist.

Additionally, the present study used a lumped representation of the whole city land surface dynamics using a simplified single park and urban canyon approach, that neglects within city heterogeneities. As demonstrated with the London example, a lumped scale simulation can provide good estimates of city average SUHI and CUHI intensities, however it cannot estimate within city variability, which is significant, especially if large variations in city morphology exist. Those finer-scale results could further guide the selection of locations where representative measurement stations should be placed, providing information for long-term projects as for example BUBBLE (Rotach et al., 2005).

Our approach also does not resolve the atmospheric and boundary layer dynamics within a city. To fully understand the development of UHI_{both} and associated feedbacks, a full urban climate model combined with a detailed land surface scheme as the UT&C model would be necessary, even though results obtained in this study suggest that dominant effects on surface and near-surface temperature can be captured well with an uncoupled urban canyon model. Previous studies used urban climate models such as urban WRF (Li et al., 2014; Touchaei and Wang, 2015; Georgescu et al., 2011), or reduced complexity models such as UrbClim (Zhou et al., 2016a) for a detailed description of atmospheric dynamics within cities. Coupling of urban land surface models like UT&C with those atmospheric urban climate models, can potentially provide a way forward to quantify the role of city heterogeneities, albeit with

a considerable increase in computational demand.

5. Conclusion

A state-of-the-art urban ecohydrological model (UT&C), parametrized with multi-source remote sensing data, was used to investigate the canopy and surface urban heat island (CUHI and SUHI) effect in 49 North-hemisphere large urban clusters characterized by different background climates. Using such an approach, our simulations could robustly reproduce the observed dynamics of SUHI viewed from above in different climates. Our study shows that summer ground-level pedestrian SUHI and CUHI are both dependent on the city's background climate, with daytime UHIs both decreasing with aridity level and nighttime UHIs both following the opposite patterns. More humid cities experience higher daytime SUHIs and CUHIs, which was predominantly caused by a lack of evaporative cooling, related to the difference between urban-rural green cover and leaf area index. Arid cities experience higher nighttime SUHIs and CUHIs, which were attributed predominantly to the release of heat stored in buildings and ground to the urban canyon. Anthropogenic heat is a unique source of canopy air warming mainly during daytime and in arid climates due to higher energy demand for air conditioning. Urban roughness and associated heat convection within and above canyon can largely explain the difference between SUHI and CUHI development. Our results provide a mechanistic explanation and quantification of both SUHI and CUHI development in different climates and can be used to guide design to improve urban heat mitigation practices for both surface and canopy air in different regions.

CRediT authorship contribution statement

Ziyan Zhang: Conceptualization, Methodology, Validation, Formal analysis, Writing – original draft, Visualization. **Athanasios Paschalis:** Conceptualization, Methodology, Resources, Supervision. **Ana Mijic:** Writing – review & editing, Supervision, Visualization. **Naika Meili:** Software, Resources, Writing – review & editing, Visualization. **Gabriele Manoli:** Writing – review & editing, Visualization, Conceptualization. **Maarten van Reeuwijk:** Writing – review & editing, Conceptualization. **Simone Fatichi:** Writing – review & editing, Visualization.

Declaration of Competing Interest

The authors declare no conflict of interest.

Acknowledgements

We thank Prof Bou-Zeid and other three anonymous reviewers for their very constructive comments that significantly improved our manuscript. ZZ, AM and AP acknowledge support from the NERC funded CAMELLIA project (Community Water Management for a Liveable London) in London (NE/S003495/1). NM and SF acknowledge the support of the National University of Singapore through the project "Bridging scales from below: The role of heterogeneities in the global water and carbon budgets" (22-3637-A0001). GM acknowledges support by "The Branco Weiss Fellowship – Society in Science" administered by ETH Zurich.

The code for UT&C model is archive in Zenodo (Meili and Fatichi, 2019) and can be downloaded from https://zenodo.org/record/3548147#.YoYVvaiZOUl. Other data or model used in this study and their download links are:

- ERA5-Land hourly data (https://cds.climate.copernicus.eu/cdsapp#!/dataset/reanalysis-era5-land?tab=overview)
- City Clusters (https://drive.google.com/drive/folders/1yzcoRAjjubiLDqlg6zbLUCfE_m1mHAsL?usp=sharing)
- Building height (https://landbigdata.github.io/cscproject/)
- OpenStreetMap (https://download.geofabrik.de/)
- Land use fraction (https://land.copernicus.eu/global/products/lc)
- Impervious land fraction (https://sedac.ciesin.columbia.edu/data/set/ulandsat-gmis-v1/data-download)
- SoilGrids (https://maps.isric.org/)
- TRY dataset (https://www.try-db.org/TryWeb/Home.php)
- LAI (https://land.copernicus.eu/global/products/lai)
- V_{cmax} (Walker et al., 2021) (https://ngt-data.lbl.gov/dois/NGT0114/)
- ϕ_s when plant water uptake downregulates from its maximum rate due to water stress (Bassiouni, 2020) (https://zenodo.org/record/3605620#.YoTzlaiZOUk)
- LUCY model (Grimmond et al., 2018) (https://researchdata.reading.ac.uk/149/)
- Geostationary Land Surface Temperature (https://land.copernicus.eu/global/products/lst)
- MODIS Land Surface Temperature (https://modis.gsfc.nasa.gov/data/dataprod/mod11.php)

Appendix A. Supplementary data

Supplementary data to this article can be found online at https://doi.org/10.1016/j.uclim.2022.101215.

References

Allen, L., Lindberg, F., Grimmond, C.S.B., 2011. Global to city scale urban anthropogenic heat flux: model and variability. Int. J. Climatol. 31 (13), 1990–2005. Available from: https://doi.org/10.1002/joc.2210.

Arnfield, A.J., 2003. Two decades of urban climate research: a review of turbulence, exchanges of energy and water, and the urban heat island. Int. J. Climatol. 23 (1), 1–26. Available from. https://doi.org/10.1002/joc.859 (Accessed: 16 July 2020).

Ban-Weiss, G.A., Woods, J., Levinson, R., 2015. Using remote sensing to quantify albedo of roofs in seven California cities, Part 1: Methods. Sol. Energy 115, 777–790. Available from. https://doi.org/10.1016/j.solener.2014.10.022 (Accessed: 20 January 2022).

Bassiouni, M., 2020. *Global dataset of ecohydrological parameters inferred from satellite observations, version V2.0*. 2020. Zenodo. Available from: https://zenodo.org/record/3605620#.YoTzlaiZOUk.

Bassiouni, M., Good, S.P., Still, C.J., Higgins, C.W., 2020. Plant Water Uptake Thresholds Inferred From Satellite Soile Moisture. Geophys. Res. Lett. 47 (7) https://doi.org/10.1029/2020GL087077 e2020GL087077. Available from. (Accessed: 16 March 2021).

Broadbent, A.M., Coutts, A.M., Tapper, N.J., Demuzere, M., 2018. The cooling effect of irrigation on urban microclimate during heatwave conditions. Urban Clim. 23, 309–329. Available from. https://doi.org/10.1016/j.uclim.2017.05.002. Accessed: 17 June 2021.

Brown de Colstoun, E.C., Huang, C., Wang, P., Tilton, J.C., et al. (2017) *Global Man-made Impervious Surface (GMIS) Dataset From Landsat*. 2017. NASA Socioeconomic Data and Applications Center (SEDAC). Available from: https://doi.org/https://doi.org/10.7927/H4P55KKF.

Buchhorn, M., Smets, B., Bertels, L., Lesiv, M., et al. (2019) Land Monitoring Service. Version V2. 0.2 Available from: doi:https://doi.org/10.5281/zenodo.3243509.

Cao, C., Lee, X., Liu, S., Schultz, N., et al., 2016. Urban heat islands in China enhanced by haze pollution. Nat. Commun. 7 (1), 1–7. Available from. https://doi.org/10.1038/ncomms12509.

Chakraborty, T., Lee, X., 2019. A simplified urban-extent algorithm to characterize surface urban heat islands on a global scale and examine vegetation control on their spatiotemporal variability. Int. J. Appl. Earth Obs. Geoinf. 74, 269–280. Available from. https://doi.org/10.1016/j.jag.2018.09.015 (Accessed: 24 May 2021.

Chakraborty, T., Sarangi, C., Tripathi, S.N., 2017. Understanding Diurnality and inter-seasonality of a sub-tropical urban Heat Island. Bound.-Layer Meteorol. 163 (2), 287–309. Available from. https://doi.org/10.1007/s10546-016-0223-0. Accessed: 28 February 2022.

Chapman, L., Bell, C., Bell, S., 2017. Can the crowdsourcing data paradigm take atmospheric science to a new level? A case study of the urban heat island of London quantified using Netatmo weather stations. Int. J. Climatol. 37 (9), 3597–3605. Available from. https://doi.org/10.1002/joc.4940.

Chen, L., Ng, E., An, X., Ren, C., et al., 2012. Sky view factor analysis of street canyons and its implications for daytime intra-urban air temperature differentials in high-rise, high-density urban areas of Hong Kong: a GIS-based simulation approach. Int. J. Climatol. 32 (1), 121–136. Available from. https://doi.org/10.1002/joc.2243 (Accessed: 30 March 2022).

Chew, L.W., Liu, X., Li, X.X., Norford, L.K., 2021. Interaction between heat wave and urban heat island: a case study in a tropical coastal city, Singapore. Atmos. Res. 247, 105134. Available from. https://doi.org/10.1016/j.atmosres.2020.105134.

Chow, W.T.L., Pope, R.L., Martin, C.A., Brazel, A.J., 2011. Observing and modeling the nocturnal park cool island of an arid city: horizontal and vertical impacts. Theor. Appl. Climatol. 103 (1–2), 197–211. Available from. https://doi.org/10.1007/s00704-010-0293-8 (Accessed: 1 March 2022).

Chow, W.T.L., Volo, T.J., Vivoni, E.R., Jenerette, G.D., et al., 2014. Seasonal dynamics of a suburban energy balance in Phoenix, Arizona. Int. J. Climatol. 34 (15), 3863–3880. Available from. https://doi.org/10.1002/joc.3947. Accessed: 27 July 2020.

Coutts, A.M., Tapper, N.J., Beringer, J., Loughnan, M., et al., 2013. Watering our cities: the capacity for water sensitive Urban Design to support urban cooling and improve human thermal comfort in the Australian context. Prog. Phys. Geogr. 37 (1), 2–28. Available from. https://doi.org/10.1177/0309133312461032 (Accessed: 29 March 2022).

Cui, Y.Y., De Foy, B., 2012. Seasonal variations of the urban heat island at the surface and the near-surface and reductions due to urban vegetation in Mexico City. J. Appl. Meteorol. Climatol. 51 (5), 855–868. Available from. https://doi.org/10.1175/JAMC-D-11-0104.1 (Accessed: 6 March 2022).

De Pury, D.G.G., Farquhar, G.D., 1997. Simple scaling of photosynthesis from leaves to canopies without the errors of big-leaf models. Plant Cell Environ. 20 (5), 537–557. Available from. https://doi.org/10.1111/j.1365-3040.1997.00094.x (Accessed: 29 March 2022).

de Sousa, L.M., Poggio, L., Batjes, N.H., Heuvelink, G.B.M., et al., 2020. SoilGrids 2.0: producing quality-assessed soil information for the globe [in review]. Soil. https://doi.org/10.5194/soil-2020-65. Available from.

Fan, Y., Li, Y., Bejan, A., Wang, Y., et al., 2017. Horizontal extent of the urban heat dome flow. Sci. Rep. 7 (1), 11681. Available from. https://doi.org/10.1038/s41598-017-09917-4 (Accessed: 20 January 2022).

Fatichi, S., Ivanov, V.Y., Caporali, E., 2012a. A mechanistic ecohydrological model to investigate complex interactions in cold and warm water-controlled environments: 1. Theoretical framework and plot-scale analysis. J. Adv. Model. Earth Syst. 4 (2) https://doi.org/10.1029/2011MS000086. Available from.

Fatichi, S., Ivanov, V.Y., Caporali, E., 2012b. A mechanistic ecohydrological model to investigate complex interactions in cold and warm water-controlled environments: 2. Spatiotemporal analyses. J. Adv. Model. Earth Syst. 4 (5), 5003. Available from. https://doi.org/10.1029/2011MS000087 (Accessed: 18 March 2022).

Fitria, R., Kim, D., Baik, J., Choi, M., 2019. Impact of biophysical mechanisms on urban Heat Island associated with climate variation and urban morphology. Sci. Rep. 9 (1), 1–13. Available from. https://doi.org/10.1038/s41598-019-55847-8 (Accessed: 23 February 2022).

Frank, A., Heidemann, W., Spindler, K., 2016. Modeling of the surface-to-surface radiation exchange using a Monte Carlo method. J. Phys. Conf. Ser. 21 https://doi.org/10.1088/1742-6596/745/3/032143. October 2016 Institute of Physics publishing. p. 39. Available from. (Accessed: 28 June 2021).

Freitas, S.C., Trigo, I.F., Macedo, J., Barroso, C., et al., 2013. Land surface temperature from multiple geostationary satellites. Int. J. Remote Sens. 34 (9–10), 3051–3068. Available from. https://doi.org/10.1080/01431161.2012.716925 (Accessed: 18 May 2022).

Freni, G., Liuzzo, L., 2019. Effectiveness of rainwater harvesting systems for flood reduction in residential urban areas. Water (Switzerland) 11 (7), 1389. Available from. https://doi.org/10.3390/w11071389 (Accessed: 18 June 2021).

Fuster, B., Sánchez-Zapero, J., Camacho, F., García-Santos, V., et al., 2020. Quality assessment of PROBA-V LAI, fAPAR and fCOVER collection 300 m products of Copernicus global land service. Remote Sens. 12 (6), 1017. Available from. https://doi.org/10.3390/rs12061017 (Accessed: 22 March 2021).

Gago, E.J., Roldan, J., Pacheco-Torres, R., Ordóñez, J., 2013. The city and urban heat islands: a review of strategies to mitigate adverse effects. Renew. Sust. Energ. Rev. 25, 749–758. Available from. https://doi.org/10.1016/j.rser.2013.05.057 (Accessed: 22 March 2022).

Georgescu, M., Moustaoui, M., Mahalov, A., Dudhia, J., 2011. An alternative explanation of the semiarid urban area "oasis effect". J. Geophys. Res.-Atmos. 116 (D24) https://doi.org/10.1029/2011JD016720 n/a-n/a. Available from.

Giannaros, C., Nenes, A., Giannaros, T.M., Kourtidis, K., et al., 2018. A comprehensive approach for the simulation of the urban Heat Island effect with the WRF/SLUCM modeling system: the case of Athens (Greece). Atmos. Res. 201, 86–101. Available from. https://doi.org/10.1016/j.atmosres.2017.10.015. Accessed: 2 July 2021.

Greater London Authority, 2015. *Statistical GIS Boundary for London*. 2015. Greater London Authority. Available from: https://data.london.gov.uk/dataset/statistical-gis-boundary-files-london (Accessed: 20 October 2021).

Greater London Authority, 2021. Local Authority Maintained Trees. 2021. Available from: https://data.london.gov.uk/dataset/local-authority-maintained-trees (Accessed: 12 July 2021).

Grimmond, C.S.B., Blackett, M., Best, M.J., Barlow, J., et al., 2010. The international urban energy balance models comparison project: first results from phase 1. J. Appl. Meteorol. Climatol. 49 (6), 1268–1292. Available from. https://doi.org/10.1175/2010JAMC2354.1.

Grimmond, S., Lindberg, F., Allen, L., Yogeswaran, N., et al., 2018. *LUCY: Large scale Urban Consumption of Energy*. 2018. University of Reading. https://doi.org/10.17864/1947.149.

Grylls, T., van Reeuwijk, M., 2021. Tree model with drag, transpiration, shading and deposition: identification of cooling regimes and large-eddy simulation. Agric. For. Meteorol. 298–299, 108288. Available from. https://doi.org/10.1016/j.agrformet.2020.108288 (Accessed: 28 February 2022).

Gu, Y., Li, D., 2018. A modeling study of the sensitivity of urban heat islands to precipitation at climate scales. Urban Clim. 24, 982–993. Available from. https://doi.org/10.1016/j.uclim.2017.12.001 (Accessed: 8 June 2021).
Hamdi, R., Schayes, G., 2008. Sensitivity study of the urban heat island intensity to urban characteristics. Int. J. Climatol. 28 (7), 973–982. Available from. https://doi.org/10.1002/joc.1598.
He, B.-J., 2019. Towards the next generation of green building for urban heat island mitigation: zero UHI impact building. Sustain. Cities Soc. 50, 101647. Available from. https://doi.org/10.1016/j.scs.2019.101647 (Accessed: 21 March 2022).
Hengl, T., De Jesus, J.M., Heuvelink, G.B.M., Gonzalez, M.R., et al., 2017. SoilGrids250m: global gridded soil information based on machine learning. PLoS One 12 (2), e0169748. Available from. https://doi.org/10.1371/journal.pone.0169748 (Accessed: 28 June 2021).
Ho, H.C., Knudby, A., Xu, Y., Hodul, M., et al., 2016. A comparison of urban heat islands mapped using skin temperature, air temperature, and apparent temperature (humidex), for the greater Vancouver area. Sci. Total Environ. 544, 929–938. Available from. https://doi.org/10.1016/j.scitotenv.2015.12.021. Accessed: 19 January 2022.
Hoang, L., Fenner, R.A., 2016. System interactions of stormwater management using sustainable urban drainage systems and green infrastructure. Urban Water J. 13 (7), 739–758. Available from. https://doi.org/10.1080/1573062X.2015.1036083.
Howell, J.R., 1969. Application of Monte Carlo to heat transfer problems. Adv. Heat Tran. 5 (C), 1–54. Available from. https://doi.org/10.1016/S0065-2717(08)70128-X.
Howell, J.R., 1998. The Monte Carlo method in radiative heat transfer. In: American Society of Mechanical Engineers, heat transfer division, 1998. HTD, pp. 1–19. Available from: https://asmedigitalcollection.asme.org/heattransfer/article/120/3/547/430215?casa_token=m7QBZu_OCnUAAAAA:EmJiIK4ATHRsFA8RSdimK22NLTgt-45qThL0EwrcnMQazkceS3jRB5lD3auLK5vHSnzfE0U2 (Accessed: 28 June 2021).
Howells, M., Hermann, S., Welsch, M., Bazilian, M., et al., 2013. Integrated analysis of climate change, land-use, energy and water strategies. Nat. Clim. Chang. 3 (7), 621–626. Available from. https://doi.org/10.1038/nclimate1789. Accessed: 17 June 2021.
Huang, X., Song, J., Wang, C., Chui, T.F.M., et al., 2021. The synergistic effect of urban heat and moisture islands in a compact high-rise city. Build. Environ. 205, 108274. Available from. https://doi.org/10.1016/j.buildenv.2021.108274 (Accessed: 1 March 2022).
Ibsen, P.C., Borowy, D., Dell, T., Greydanus, H., et al., 2021. Greater aridity increases the magnitude of urban nighttime vegetation-derived air cooling. Environ. Res. Lett. 16 (3), 034011. Available from. https://doi.org/10.1088/1748-9326/abdf8a (Accessed: 3 March 2022).
Imran, H.M., Kala, J., Ng, A.W.M., Muthukumaran, S., 2019. Impacts of future urban expansion on urban heat island effects during heatwave events in the city of Melbourne in Southeast Australia. Q. J. R. Meteorol. Soc. 145 (723), 2586–2602. Available from. https://doi.org/10.1002/qj.3580 (Accessed: 22 March 2022).
Jacobs, S.J., Gallant, A.J.E., Tapper, N.J., Li, D., 2018. Use of Cool Roofs and Vegetation to Mitigate Urban Heat and Improve Human Thermal Stress in Melbourne, Australia. J. Appl. Meteorol. Climatol. 57 (8), 1747–1764. Available from.
Kattge, J., Díaz, S., Lavorel, S., Prentice, I.C., et al., 2011. TRY – a global database of plant traits. Glob. Chang. Biol. 17, 2905–2935.
Kolokotroni, M., Giridharan, R., 2008. Urban heat island intensity in London: An investigation of the impact of physical characteristics on changes in outdoor air temperature during summer. Sol. Energy 82 (11), 986–998. Available from. https://doi.org/10.1016/j.solener.2008.05.004. Accessed: 12 July 2021.
Kottek, M., Grieser, J., Beck, C., Rudolf, B., et al., 2006. World map of the Köppen-Geiger climate classification updated. Meteorol. Z. 15 (3), 259–263. Available from. https://doi.org/10.1127/0941-2948/2006/0130. Accessed: 6 July 2021.
Kotthaus, S., Grimmond, C.S.B., 2012. Identification of Micro-scale anthropogenic CO2, heat and moisture sources – processing eddy covariance fluxes for a dense urban environment. Atmos. Environ. 57, 301–316. Available from. https://doi.org/10.1016/j.atmosenv.2012.04.024. Accessed: 27 July 2020.
Krayenhoff, E.S., Jiang, T., Christen, A., Martilli, A., et al., 2020. A multi-layer urban canopy meteorological model with trees (BEP-tree): street tree impacts on pedestrian-level climate. Urban Clim. 32, 100590. Available from. https://doi.org/10.1016/j.uclim.2020.100590.
Krüger, E., Emmanuel, R., 2013. Accounting for atmospheric stability conditions in urban heat island studies: the case of Glasgow, UK. Landsc. Urban Plan. 117, 112–121. Available from. https://doi.org/10.1016/j.landurbplan.2013.04.019.
Kumar, R., Mishra, V., Buzan, J., Kumar, R., et al., 2017. Dominant control of agriculture and irrigation on urban heat island in India. Sci. Rep. 7 (1), 14054. Available from. https://doi.org/10.1038/s41598-017-14213-2 (Accessed: 2 October 2020).
Leuning, R., 1995. A critical appraisal of a combined stomatal-photosynthesis model for C3 plants. Plant Cell Environ. 18 (4), 339–355. Available from. https://doi.org/10.1111/j.1365-3040.1995.tb00370.x. Accessed: 29 June 2020.
Li, D., Bou-Zeid, E., Oppenheimer, M., 2014. The effectiveness of cool and green roofs as urban heat island mitigation strategies. Environ. Res. Lett. 9 (5), 55002. Available from. https://doi.org/10.1088/1748-9326/9/5/055002 (Accessed: 22 March 2021).
Li, D., Liao, W., Rigden, A.J., Liu, X., et al., 2019. Urban heat island: aerodynamics or imperviousness? Sci. Adv. 5 (4), eaau4299. Available from. https://doi.org/10.1126/sciadv.aau4299.
Li, M., Koks, E., Taubenböck, H., van Vliet, J., 2020. Continental-scale mapping and analysis of 3D building structure. Remote Sens. Environ. 245, 111859. Available from. https://doi.org/10.1016/j.rse.2020.111859.
Liao, W., Liu, X., Li, D., Luo, M., et al., 2018. Stronger contributions of urbanization to heat wave trends in wet climates. Geophys. Res. Lett. 45 (20), 11,310–11,317. Available from. https://doi.org/10.1029/2018GL079679. Accessed: 8 June 2021.
Lin, P., Lau, S.S.Y., Qin, H., Gou, Z., 2017. Effects of urban planning indicators on urban heat island: a case study of pocket parks in high-rise high-density environment. Landsc. Urban Plan. 168, 48–60. Available from. https://doi.org/10.1016/j.landurbplan.2017.09.024.
Lindberg, F., Grimmond, C.S.B., Yogeswaran, N., Kotthaus, S., et al., 2013. Impact of city changes and weather on anthropogenic heat flux in Europe 1995-2015. Urban Clim. 4, 1–15. Available from. https://doi.org/10.1016/j.uclim.2013.03.002.
Liu, L., Jensen, M.B., 2018. Green infrastructure for sustainable urban water management: practices of five forerunner cities. Cities. 74, 126–133. Available from. https://doi.org/10.1016/j.cities.2017.11.013.
Liu, L., Lin, Y., Liu, J., Wang, L., et al., 2017. Analysis of local-scale urban heat island characteristics using an integrated method of mobile measurement and GIS-based spatial interpolation. Build. Environ. 117, 191–207. Available from. https://doi.org/10.1016/j.buildenv.2017.03.013 (Accessed: 2 July 2021).
Liu, L., Fryd, O., Zhang, S., 2019. Blue-green infrastructure for sustainable urban stormwater management-lessons from six municipality-led pilot projects in Beijing and Copenhagen. Water (Switzerland) 11 (10), 2024. Available from.
Liu, Y., Li, Q., Yang, L., Mu, K., et al., 2020. Urban heat island effects of various urban morphologies under regional climate conditions. Sci. Total Environ. 743, 140589. Available from. https://doi.org/10.1016/j.scitotenv.2020.140589 (Accessed: 22 February 2022).
Mahat, V., Tarboton, D.G., Molotch, N.P., 2013. Testing above- and below-canopy representations of turbulent fluxes in an energy balance snowmelt model. Water Resour. Res. 49 (2), 1107–1122. Available from. https://doi.org/10.1002/wrcr.20073 (Accessed: 1 July 2021).
Manoli, G., Fatichi, S., Schläpfer, M., Yu, K., et al., 2019. Magnitude of urban heat islands largely explained by climate and population. Nature 573 (7772), 55–60. Available from. https://doi.org/10.1038/s41586-019-1512-9 (Accessed: 16 July 2020).
Manoli, G., Fatichi, S., Bou-Zeid, E., Katul, G.G., 2020. Seasonal hysteresis of surface urban heat islands. Proc. Natl. Acad. Sci. 117 (13), 7082–7089. Available from. https://doi.org/10.1073/pnas.1917554117 (Accessed: 16 July 2020).
Mascart, P., Noilhan, J., Giordani, H., 1995. A modified parameterization of flux-profile relationships in the surface layer using different roughness length values for heat and momentum. Bound.-Layer Meteorol. 72 (4), 331–344. Available from. https://doi.org/10.1007/BF00708998.
Meier, F., Fenner, D., Grassmann, T., Otto, M., et al., 2017. Crowdsourcing air temperature from citizen weather stations for urban climate research. Urban Clim. 19, 170–191. Available from. https://doi.org/10.1016/J.UCLIM.2017.01.006.
Meili, N., Fatichi, S., 2019. *Urban Tethys-Chloris (UT&C v1.0) with the possibility of sub-hourly time steps*. 20 November 2019. Zenodo. Available from. https://doi.org/10.5281/ZENODO.3548147 (Accessed: 18 May 2022).
Meili, N., Manoli, G., Burlando, P., Bou-Zeid, E., et al., 2020. An urban ecohydrological model to quantify the effect of vegetation on urban climate and hydrology (UT&C v1.0). Geosci. Model Dev. 13 (1), 335–362. Available from. https://doi.org/10.5194/gmd-13-335-2020.
Meili, N., Acero, J.A., Peleg, N., Manoli, G., et al. (2021a) Vegetation cover and plant-trait effects on outdoor thermal comfort in a tropical city. *Building and environment* 195, 107733. Available from: doi:https://doi.org/10.1016/j.buildenv.2021.107733 (Accessed: 13 October 2021).

Meili, N., Manoli, G., Burlando, P., Carmeliet, J., et al., 2021b. Tree effects on urban microclimate: diurnal, seasonal, and climatic temperature differences explained by separating radiation, evapotranspiration, and roughness effects. Urban For. Urban Green. 58, 126970. Available from. https://doi.org/10.1016/j.ufug.2020.126970 (Accessed: 13 January 2021).

Moradi, M., Krayenhoff, E.S., Aliabadi, A.A., 2022. A comprehensive indoor–outdoor urban climate model with hydrology: the Vertical City weather generator (VCWG v2.0.0). Build. Environ. 207, 108406. Available from. https://doi.org/10.1016/j.buildenv.2021.108406.

Moustakis, Y., Fatichi, S., Onof, C., Paschalis, A., 2022. Insensitivity of ecosystem productivity to predicted changes in fine-scale rainfall variability. J. Geophys. Res. Biogeosci. 127 (2), e2021JG006735. Available from. https://doi.org/10.1029/2021jg006735 (Accessed: 18 March 2022).

Muftah, H., Rowan, T.S.L., Butler, A.P., 2021. Towards open-source LOD2 modelling using convolutional neural networks. Mode. Earth Syst. Environ. 1, 3. Available from. https://doi.org/10.1007/s40808-021-01159-8. Accessed: 2 July 2021).

Muñoz Sabater, J., 2019. *ERA5-Land hourly data from 1981 to present. Copernicus Climate Change Service (C3S) Climate Data Store (CDS)*. 2019. Available from:. https://doi.org/10.24381/cds.e2161bac.

Novick, K.A., Katul, G.G., 2020. The duality of reforestation impacts on surface and air temperature. J. Geophys. Res. Biogeosci. 125 (4), e2019JG005543. Available from. https://doi.org/10.1029/2019JG005543 (Accessed: 7 March 2022).

Oke, T.R., 1982. The energetic basis of the urban heat island. Q. J. R. Meteorol. Soc. 108 (455), 1–24. Available from. https://doi.org/10.1002/qj.49710845502 (Accessed: 16 July 2020).

Oke, T.R., 1995. The Heat Island of the urban boundary layer: characteristics, causes and effects. In: wind climate in cities. Springer, pp. 81–107. Available from. https://doi.org/10.1007/978-94-017-3686-2_5.

Oke, T.R., Mills, G., Christen, A., Voogt, J.A., 2017. Urban Climates. Cambridge University Press, Cambridge. https://doi.org/10.1017/9781139016476. Available from:

Omidvar, H., Bou-Zeid, E., Li, Q., Mellado, J.-P., et al., 2020. Plume or bubble? Mixed-convection flow regimes and city-scale circulations. J. Fluid Mech. 897, A5. Available from. https://doi.org/10.1017/jfm.2020.360. Accessed: 20 January 2022).

Overeem, A., Robinson, J.C., Leijnse, H., Steeneveld, G.J., et al., 2013. Crowdsourcing urban air temperatures from smartphone battery temperatures. Geophys. Res. Lett. 40 (15), 4081–4085. Available from. https://doi.org/10.1002/grl.50786 (Accessed: 2 July 2021).

Paschalis, A., Katul, G.G., Fatichi, S., Palmroth, S., et al., 2017. On the variability of the ecosystem response to elevated atmospheric CO2 across spatial and temporal scales at the Duke Forest FACE experiment. Agric. For. Meteorol. 232, 367–383. Available from. https://doi.org/10.1016/j.agrformet.2016.09.003 (Accessed: 29 June 2020).

Paschalis, A., Fatichi, S., Pappas, C., Or, D., 2018. Covariation of vegetation and climate constrains present and future T/ET variability. Environ. Res. Lett. 13 (10), 104012. Available from. https://doi.org/10.1088/1748-9326/aae267 (Accessed: 29 June 2020).

Paschalis, A., Chakraborty, T., Fatichi, S., Meili, N., et al., 2021. Urban forests as Main regulator of the evaporative cooling effect in cities. AGU Adv. 2 (2), e2020AV000303. Available from. https://doi.org/10.1029/2020AV000303 (Accessed: 24 May 2021).

Peng, S., Piao, S., Ciais, P., Friedlingstein, P., et al., 2012. Surface urban heat island across 419 global big cities. Environ. Sci. Technol. 46 (2), 696–703. Available from. https://doi.org/10.1021/es2030438 (Accessed: 4 February 2021).

Rahman, M.A., Moser, A., Rötzer, T., Pauleit, S., 2019. Comparing the transpirational and shading effects of two contrasting urban tree species. Urban Ecosyst. 22 (4), 683–697. Available from. https://doi.org/10.1007/s11252-019-00853-x (Accessed: 22 March 2021.

Reyes, B., Hogue, T., Maxwell, R., 2018. Urban irrigation suppresses land surface temperature and changes the hydrologic regime in semi-arid regions. Water 10 (11), 1563. Available from. https://doi.org/10.3390/w10111563 (Accessed: 18 June 2021).

Rotach, M.W., Vogt, R., Bernhofer, C., Batchvarova, E., et al. (2005) BUBBLE - An urban boundary layer meteorology project. *Theor. Appl. Climatol.* 81 (3–4), 231–261. Available from: doi:https://doi.org/10.1007/s00704-004-0117-9.

Rowley, F.B. & Eckley, W.A. (1932) Surface coefficients as affected by wind direction. *ASHREA Trans* (39), 33–46. Available from: https://scholar.google.co.uk/scholar?hl=en&as_sdt=0%2C5&q=Surface+conductance+as+affected+by+air+velocity%2C+temperature+and+character+of+surface&btnG Accessed: 1 July 2021).

Rowley, F.B., Algren, A.B. & Blackshaw, J. (1930) Surface conductance as affected by air velocity, temperature and character of surface. *ASHREA Trans* (36), 429–446. Available from: https://scholar.google.co.uk/scholar?hl=en&as_sdt=0%2C5&q=Rowley%2C+F.+B.%2C+Algren%2C+A.+B.%2C+and+Blackshaw%2C+J.%3A+Surface+conductance+as+affected+by+air+velocity%2C+temperature+and+character+of+surface%2C+ASHREA+Trans.%2C+36%2C+429–446%2C+1930.a&btn (Accessed: 1 July 2021).

Saxton, K.E., Rawls, W.J., 2006. Soil water characteristic estimates by texture and organic matter for hydrologic solutions. Soil Sci. Soc. Am. J. 70 (5), 1569–1578. Available from. https://doi.org/10.2136/sssaj2005.0117. Accessed: 5 August 2020).

Schmutz, M., Vogt, R., Feigenwinter, C., Parlow, E., 2016. Ten years of eddy covariance measurements in Basel, Switzerland: seasonal and interannual variabilities of urban CO2 mole fraction and flux. J. Geophys. Res. 121 (14), 8649–8667. Available from. https://doi.org/10.1002/2016JD025063. Accessed: 29 March 2022).

Shuster, W.D., Schifman, L., Kelleher, C., Golden, H.E., et al., 2021. K in an urban world: new contexts for hydraulic conductivity. J. Am. Water Resour. Assoc. 57 (3), 493–504. Available from. https://doi.org/10.1111/1752-1688.12918 (Accessed: 28 June 2021).

Stewart, I.D., Krayenhoff, E.S., Voogt, J.A., Lachapelle, J.A., et al., 2021. Time evolution of the surface urban Heat Island. Earth's Future 9 (10), e2021EF002178. Available from. https://doi.org/10.1029/2021EF002178 (Accessed: 27 April 2022).

Sun, T., Sun, R., Chen, L., 2020. The trend inconsistency between land surface temperature and near surface air temperature in assessing urban Heat Island effects. Remote Sens. 12 (8), 1271. Available from. https://doi.org/10.3390/rs12081271 (Accessed: 28 February 2022).

Templeton, N.P., Vivoni, E.R., Wang, Z.-H., Schreiner-McGraw, A.P., 2018. Quantifying water and energy fluxes over different urban land covers in Phoenix, Arizona. J. Geophys. Res.-Atmos. 123 (4), 2111–2128. Available from. https://doi.org/10.1002/2017JD027845 (Accessed: 27 July 2020).

Touchaei, A.G., Wang, Y., 2015. Characterizing urban heat island in Montreal (Canada)—effect of urban morphology. Sustain. Cities Soc. 19, 395–402. Available from. https://doi.org/10.1016/j.scs.2015.03.005 (Accessed: 14 June 2021).

Varentsov, M.I., Konstantinov, P.I., Shartova, N.V., Samsonov, T.E., et al., 2020. Urban heat island of the Moscow megacity: the long-term trends and new approaches for monitoring and research based on crowdsourcing data. In: IOP Conference Series: Earth and Environmental Science, 606 (1), p. 012063. Available from. https://doi.org/10.1088/1755-1315/606/1/012063 (Accessed: 12 July 2021).

Venter, Z.S., Chakraborty, T., Lee, X., 2021. Crowdsourced air temperatures contrast satellite measures of the urban heat island and its mechanisms. Sci. Adv. 7 (22), eabb9569. Available from. https://doi.org/10.1126/sciadv.abb9569 (Accessed: 12 July 2021).

Volo, T.J., Vivoni, E.R., Martin, C.A., Earl, S., et al., 2014. Modelling soil moisture, water partitioning, and plant water stress under irrigated conditions in desert urban areas. Ecohydrology 7 (5). https://doi.org/10.1002/eco.1457 n/a-n/a. available from. (Accessed: 22 March 2021).

Walker, A.P., Quaife, T., Bodegom, P.M., De Kauwe, M.G., et al., 2017. The impact of alternative trait-scaling hypotheses for the maximum photosynthetic carboxylation rate (V cmax) on global gross primary production. New Phytol. 215 (4), 1370–1386. Available from. https://doi.org/10.1111/nph.14623 (Accessed: 16 March 2021).

Walker, A., MacBean, N., Quaife, T., van Bodegom, P., et al., 2021. *Global maximum carboxylation rate trait scaling in the Sheffield Dynamic Global Vegetation Model 1901-2012*. 2021. NGEE Tropics Data Collection. Available from. https://doi.org/10.15486/ngt/1569265.

Wan, Z., Hook, S., Hulley, G., 2015a. MOD11A1 MODIS/Terra land surface temperature/emissivity daily L3 global 1km SIN grid V006. 2015. NASA EOSDIS land processes DAAC.

Wan, Z., Hook, S., Hulley, G., 2015b. *MYD11A1 MODIS/Aqua Land Surface Temperature/Emissivity Daily L3 Global 1km SIN Grid V006*. 2015. NASA EOSDIS land processes DAAC. Available from:. https://doi.org/10.5067/MODIS/MYD11A1.006.

Wang, Z.H., 2014. Monte Carlo simulations of radiative heat exchange in a street canyon with trees. Sol. Energy 110, 704–713. Available from. https://doi.org/10.1016/j.solener.2014.10.012.

Wang, K., Jiang, S., Wang, J., Zhou, C., et al., 2017. Comparing the diurnal and seasonal variabilities of atmospheric and surface urban heat islands based on the Beijing urban meteorological network. J. Geophys. Res.-Atmos. 122 (4), 2131–2154. Available from. https://doi.org/10.1002/2016JD025304 (Accessed: 28 February 2022).

Wang, S., Ju, W., Peñuelas, J., Cescatti, A., et al., 2019. Urban−rural gradients reveal joint control of elevated CO2 and temperature on extended photosynthetic seasons. Nat. Ecol. Evol. 3 (7), 1076–1085. Available from. https://doi.org/10.1038/s41559-019-0931-1 (Accessed: 29 June 2020).

Wang, L., Li, D., Zhang, N., Sun, J., et al., 2020. Surface urban heat and cool islands and their drivers: An observational study in Nanjing, China. J. Appl. Meteorol. Climatol. 59 (12), 1987–2000. Available from. https://doi.org/10.1175/JAMC-D-20-0089.1 (Accessed: 23 February 2022).

Wang, C., Wang, Z.-H., Ryu, Y.-H., 2021. A single-layer urban canopy model with transmissive radiation exchange between trees and street canyons. Build. Environ. 191, 107593. Available from. https://doi.org/10.1016/j.buildenv.2021.107593 (Accessed: 1 March 2022).

Warren, E.L., Young, D.T., Chapman, L., Muller, C., et al., 2016. The Birmingham urban climate laboratory-a high density, urban meteorological dataset, from 2012-2014. Scientific Data 3 (1), 1–8. Available from. https://doi.org/10.1038/sdata.2016.38 (Accessed: 19 October 2021).

Wood, C.R., Kouznetsov, R.D., Gierens, R., Nordbo, A., et al., 2013. On the Temperature Structure Parameter and Sensible Heat Flux over Helsinki from Sonic Anemometry and Scintillometry. J. Atmos. Ocean. Technol. 30 (8), 1604–1615. Available from. https://doi.org/10.1175/JTECH-D-12-00209.1 (Accessed: 27 July 2020).

Yang, Q., Huang, X., Tang, Q., 2020a. Irrigation cooling effect on land surface temperature across China based on satellite observations. Sci. Total Environ. 705, 135984. Available from. https://doi.org/10.1016/j.scitotenv.2019.135984 (Accessed: 2 October 2020).

Yang, J., Wong, M.S., Ho, H.C., Krayenhoff, E.S., et al., 2020b. A semi-empirical method for estimating complete surface temperature from radiometric surface temperature, a study in Hong Kong city. Remote Sens. Environ. 237, 111540. Available from. https://doi.org/10.1016/j.rse.2019.111540 (Accessed: 28 February 2022).

Yang, J., Menenti, M., Wu, Z., Wong, M.S., et al., 2021. Assessing the impact of urban geometry on surface urban heat island using complete and nadir temperatures. Int. J. Climatol. 41 (S1), E3219–E3238. Available from. https://doi.org/10.1002/joc.6919 (Accessed: 28 February 2022).

Yu, Z., Chen, S., Wong, N.H., 2020. Temporal variation in the impact of urban morphology on outdoor air temperature in the tropics: a campus case study. Build. Environ. 181, 107132. Available from. https://doi.org/10.1016/J.BUILDENV.2020.107132.

Zhang, H., Zhang, H., 2015. Comparison of turbulent sensible heat flux determined by large-aperture Scintillometer and Eddy covariance over urban and suburban areas. Bound.-Layer Meteorol. 154 (1), 119–136. Available from. https://doi.org/10.1007/s10546-014-9965-8 (Accessed: 27 July 2020).

Zhang, N., Wang, X., Peng, Z., 2014. Large-Eddy simulation of mesoscale circulations forced by inhomogeneous urban Heat Island. Bound.-Layer Meteorol. 151 (1), 179–194. Available from. https://doi.org/10.1007/s10546-013-9879-x (Accessed: 20 January 2022).

Zhang, Z., Paschalis, A., Mijic, A., 2021. Planning London's green spaces in an integrated water management approach to enhance future resilience in urban stormwater control. J. Hydrol. 126126. Available from. https://doi.org/10.1016/j.jhydrol.2021.126126 (Accessed: 11 March 2021).

Zhao, L., Lee, X., Smith, R.B., Oleson, K., 2014. Strong contributions of local background climate to urban heat islands. Nature 511 (7508), 216–219. Available from. https://doi.org/10.1038/nature13462 (Accessed: 1 September 2020).

Zhao, L., Oppenheimer, M., Zhu, Q., Baldwin, J.W., et al., 2018. Interactions between urban heat islands and heat waves. Environ. Res. Lett. 13 (3), 034003. Available from. https://doi.org/10.1088/1748-9326/aa9f73.

Zhou, B., Rybski, D., Kropp, J.P., 2013. On the statistics of urban heat island intensity. Geophys. Res. Lett. 40 (20), 5486–5491. Available from. https://doi.org/10.1002/2013GL057320 (Accessed: 16 July 2020).

Zhou, D., Zhao, S., Liu, S., Zhang, L., et al., 2014. Surface urban heat island in China's 32 major cities: spatial patterns and drivers. Remote Sens. Environ. 152, 51–61. Available from. https://doi.org/10.1016/j.rse.2014.05.017.

Zhou, B., Lauwaet, D., Hooyberghs, H., De Ridder, K., et al., 2016a. Assessing seasonality in the surface urban Heat Island of London. J. Appl. Meteorol. Climatol. 55 (3), 493–505. Available from. https://doi.org/10.1175/JAMC-D-15-0041.1 (Accessed: 2 October 2020).

Zhou, D., Zhang, L., Li, D., Huang, D., et al., 2016b. Climate–vegetation control on the diurnal and seasonal variations of surface urban heat islands in China. Environ. Res. Lett. 11 (7), 074009. Available from. https://doi.org/10.1088/1748-9326/11/7/074009. Accessed: 8 June 2021).

Zhou, D., Xiao, J., Bonafoni, S., Berger, C., et al., 2018. Satellite remote sensing of surface urban Heat Islands: Progress, challenges, and perspectives. Remote Sens. 11 (1), 48. Available from. https://doi.org/10.3390/rs11010048 (Accessed: 22 March 2021).

Ziter, C.D., Pedersen, E.J., Kucharik, C.J., Turner, M.G., 2019. Scale-dependent interactions between tree canopy cover and impervious surfaces reduce daytime urban heat during summer. Proc. Natl. Acad. Sci. 116 (15), 7575–7580. Available from: https://doi.org/10.1073/pnas.1817561116 (Accessed: 22 March 2021).